Turbulent thermal convection driven by free-surface evaporation in cuboidal domains of different aspect ratios

William A. Hay,[1, a)] Jimmy Martin,[2, b)] Benoît Migot,[2, c)] and Miltiadis V. Papalexandris[1, d)]
[1)] *Université catholique de Louvain, Institute of Mechanics, Materials and Civil Engineering, 1348 Louvain-la-Neuve, Belgium*
[2)] *Institut de Radioprotection et de Sûreté Nucléaire, 13115 Cadarache, St-Paul-Lez-Durance, France*

(Dated: 5 December 2020)

In this paper, we present simulations of turbulent thermal convection driven by free-surface evaporation above and a heated wall below. A novel algorithm is proposed for predicting evaporation rates at a free surface which we then validate against experimental data. At the top of a cuboidal domain, a shear-free boundary condition acts as an approximation of the free surface. We first focus on a domain of aspect ratio $\Gamma = 1$, where a fully-resolved Direct Numerical Simulation (DNS) is carried out at moderate Rayleigh number, $Ra = 1.2 \times 10^7$, and we compare flow statistics with a Large-Eddy Simulation (LES) on a coarse grid. Both the fully-resolved simulation and the LES predict well the time- and area-averaged evaporation rate and free surface temperature when compared with the experimental data. Next, we carry out a series of LES, with increasing lower wall temperature and consequently Ra. We then validate the evaporation model by comparing LES predictions of the time- and area-averaged mass flux and temperature at the upper boundary, against the experimental measurements. The aspect ratio of the domain is then reduced and we show, for the first time, the transition to a dual-roll state of the large-scale circulation (LSC) at the aspect ratio of $\Gamma = 1/4$ in a cuboidal domain. The temperature and velocity distributions at the free surface are impacted by the state of the LSC. However, we find that the water-side turbulence and aspect ratio play a negligible role on the evaporation rate above, in accordance with experimental observations.

I. INTRODUCTION

In this paper, we present a series of simulations of evaporation-driven turbulent thermal convection. With liquid water as the convecting fluid, a dynamically calculated inhomogeneous temperature gradient at a shear-free upper boundary serves as an approximation of an evaporating free surface. Building on previous publications[1,2], we first propose and validate a new evaporation algorithm before investigating whether the aspect ratio of a cuboidal domain has an influence on large-scale circulation structure, evaporation rates, mean flow properties or statistics.

Evaporation-driven thermal convection occurs in both natural sciences and in industrial flows, e.g. in Spent Fuel Pools (SFP) of nuclear facilities. With an initially quiescent velocity field in a deep water pool, evaporation at the free surface induces convective motion below. With no further heat addition, this thermal convection configuration is known as evaporative cooling. Conversely, if heat is added from below and simultaneously evacuated above then a flow is induced similar to turbulent Rayleigh-Bénard Convection (RBC). The thermal convection studied here constitutes an evaporating free-surface, adiabatic side-walls and a heated bottom wall. The problem in hand thus borrows attributes from both turbulent RBC and evaporative cooling.

Turbulent RBC is commonly studied as a fluid uniformly heated from below and cooled from above with solid upper and lower boundaries[3–5]. The flow and thermal dynamics are determined by the geometry of the system, the temperature difference across it and the resulting variation in fluid properties. The two dimensionless parameters that then govern the flow are the Prandtl, $Pr = \nu/\kappa$, and Rayleigh, $Ra = |g|\beta\Delta T H^3/(\nu\kappa)$, numbers. In these expressions, $|g|$ is the magnitude of gravitational acceleration, β the thermal expansion coefficient, H the height of the domain, ν the kinematic viscosity, ΔT the temperature difference between lower and upper boundaries and κ is the thermal diffusivity. In turbulent RBC the system response is measured in terms of the Nusselt (Nu) and Reynolds (Re) numbers[4]. The representative velocity is often that of a large-scale circulation (LSC), or mean wind, which is formed across the height of the domain. This LSC, which also exists in the evaporation-driven thermal convection configuration[1,2,6], sweeps across the upper and lower boundaries stabilizing the thermal boundary layers, and simultaneously creates a hydrodynamic boundary layer with its shear[7].

Evaporative cooling on the other hand is the study of the liquid-side flow induced by an evaporating interface[8,9] with no other heat source participating in driving the flow. The upper thermal boundary layer is then the unique source for thermal plumes in the domain. In such a thermal convection, turbulent kinetic energy peaks at the free surface[10] and the vortical turbulent structures existing beneath the interface increase in number and in magnitude as the evaporative mass flux increases[11]. Hereafter, we use the terms *interface* and *free surface* interchangeably.

Specifically, and with relation to turbulent RBC, evaporation-driven thermal convection shares the attribute of

[a)] Electronic mail: william.hay@uclouvain.be
[b)] Electronic mail: jimmy.martin@irsn.fr
[c)] Electronic mail: benoit.migot@irsn.fr
[d)] Electronic mail: miltos@uclouvain.be

plume formation at both boundaries, hence also the presence of a LSC[2]. Likewise, from evaporative cooling, the current set-up shares the attribute of the maximum rms of velocity[1,12] and temperature[2,12] fluctuations occurring at the free surface.

Our motivation is to better understand the combined effects of turbulent convection and free surface evaporation in the early stages of a loss-of-cooling accident in a SFP. Wherein, heat is added to the upper volume of the pool from the fuel assemblies below and free-surface evaporation is the main mode of phase change that leads to heat evacuation and water inventory loss. During an accident, a SFP will experience both low and high free-surface evaporation mass transfer regimes.

Post-Fukushima 2011, efforts have been made to create[13] and validate[14] models for predicting evaporative mass-transfer rates across the free surface in this high evaporation regime. Prior to this, most models were based on observations and measurements from nature, such as the evaporation taking place at the surface of lakes or oceans. Typically, the mass-transfer rate in these models was, inaccurately, a function of *bulk* water temperature and, accurately, a function of ambient air conditions, that is relative humidity and temperature. One source of error, is that in reality the mass-transfer rate depends on the free-surface temperature. It has long been known that interfacial and bulk temperatures differ as a result of free-surface evaporation[15,16], with recent research showing this difference to be substantial in the high-mass-transfer regime[14,17]. The experimental study of Boelter et al.[18] investigated evaporation in tanks up to a maximum bulk temperature of 361.15 K, and hence under high-mass transfer conditions. Importantly however, due to limitations of the experimental techniques at the time no distinction was made between free-surface and bulk temperatures. We utilise the more recent data[14] to validate our proposed algorithm for predicting evaporation rates at a free surface. To the authors knowledge, the algorithm presented herein represents the first validated model of dynamic and local free-surface evaporation in a single-phase CFD code.

The container shape and in particular, its aspect ratio, $\Gamma = W/H$ where W is the width of the cuboidal domain, plays an important role in determining the structure of the LSC. In turbulent RBC the LSC has been shown to be either in a single-roll, dual-roll or transitory state. In the single-roll state the LSC occupies the entirety of the domain, whereas under certain Ra, Pr and Γ conditions, the single-roll breaks down into a dual-roll state. One explanation for this breakdown is that the LSC is driven by plumes of the same size as the thermal boundary layers. As Ra is increased, this thickness decreases and eventually a critical Ra exists, for a given Γ and Pr, whereby hot plumes emitted from the lower wall become so thin and elongated that they lose their excess heat and thus buoyancy to the bulk fluid before reaching the cool upper boundary. At such a point the LSC sinks somewhere in the middle of the domain in order to regain heat and from the lower wall[19]. The opposite is true if the starting point is considered as the cool upper boundary and we focus on cold plumes.

In this study we fix the upper boundary surface area, so that the depth equals the width, and vary the aspect ratio via the height. In cuboidal domains at aspect ratio $\Gamma = 1$ and seemingly over a large range of Pr, the single-roll state of the LSC is dominant in thermal convection flows[2,20,21]. With respect to turbulent RBC in cylindrical domains of aspect ratio $\Gamma = 1/2$ and with water as the working fluid, the single-roll state is dominant, whereas the dual-roll state is observed only in transition. In Xi and Xia [22] it was shown that the most likely state of the LSC for aspect ratios $\Gamma = 1$ and $1/2$ is the a single-roll state, where it exists for $\sim 90\%$ and $\sim 70\%$ of the time, respectively. On the other hand, at still smaller aspect ratios, specifically $\Gamma = 1/3$, the single-roll state was shown to be present $\sim 25\%$ of the time. For the remainder, the LSC is in transition to, or actually occupying the dual-roll state . This trend suggests that any further decrease in Γ is likely to reduce further the likelihood of the single-roll state.

The single-roll state has been shown to be marginally more efficient for heat transfer than the dual-roll equivilent[23] when working in 3D geometries and with water as the working fluid. Although the difference is limited to a few percent for in domains of aspect ratio $\Gamma = 1/2$ at high Ra[24,25]. In this study, we investigate the role of aspect ratio on the LSC state, evaporation rate, mean flow properties and statistics. To the best of our knowledge, this work is the first study of its kind to assess the aforementioned subjects in slender 3D cuboidal geometries.

The paper is structured as follows: in Section II we outline the governing equations, the sub-grid scale modelling and the algorithm for calculating the temperature gradient at the upper boundary based on evaporative heat losses. Next, in Section III we present the numerical set-up and resolution criteria. In Section IV we present the results, where we first focus on the validation process. Therein, we compare the flow statistics from a direct numerical and a large-eddy simulation at moderate Ra, before comparing the evaporation model predictions with experimental results. We then present a study of the aspect ratio before drawing conclusions in Section V.

II. GOVERNING EQUATIONS

The working fluid is liquid water, which we treat as Newtonian. By not invoking the Oberbeck–Boussinesq approximation we take into account the variations of density and transport properties with temperature. For this reason, the system of governing equations is the low-Mach number approximation of the compressible Navier-Stokes-Fourier equations[26,27]. The governing equations are Favre filtered to allow for variable density Large-Eddy Simulations (LES). Applied to a generic quantity ϕ, the corresponding Favre-filtered quantity $\widetilde{\phi}$ is given as $\widetilde{\phi} = \frac{\overline{\rho\phi}}{\overline{\rho}}$, where $\overline{\rho}$ and $\overline{\rho\phi}$ are spatially filtered quantities. Accordingly, the governing equations read, in dimensional form,

$$\frac{\partial \overline{\rho}}{\partial t} + \boldsymbol{\nabla}\cdot\left(\overline{\rho}\widetilde{\boldsymbol{u}}\right) = 0\,, \tag{1}$$

$$\frac{\partial\left(\overline{\rho}\widetilde{\boldsymbol{u}}\right)}{\partial t} + \boldsymbol{\nabla}\cdot\left(\overline{\rho}\widetilde{\boldsymbol{u}}\widetilde{\boldsymbol{u}}\right) = -\boldsymbol{\nabla}\overline{p} + \boldsymbol{\nabla}\cdot\mu\left(2\widetilde{\boldsymbol{S}} - \frac{2}{3}(\boldsymbol{\nabla}\cdot\widetilde{\boldsymbol{u}})\mathbf{I}\right) - \boldsymbol{\nabla}\cdot\boldsymbol{\tau}^{\mathrm{r}} + \overline{\rho}\boldsymbol{g}\,, \tag{2}$$

$$\frac{\partial\overline{\rho}c_p\widetilde{T}}{\partial t} + \boldsymbol{\nabla}\cdot\left(\overline{\rho}c_p\widetilde{\boldsymbol{u}}\widetilde{T}\right) = \frac{\mathrm{d}p_0\left(t\right)}{\mathrm{d}t} + \boldsymbol{\nabla}\cdot\left(\lambda\boldsymbol{\nabla}\widetilde{T}\right) + \boldsymbol{\nabla}\cdot\boldsymbol{q}^{\mathrm{r}}\,, \tag{3}$$

where $\overline{\rho}$ and $\widetilde{\boldsymbol{u}} = (\widetilde{u},\widetilde{v},\widetilde{w})$ stand, respectively, for the fluid density and velocity vector. Also, $\overline{p}$ is the sum of the dynamic and bulk-viscous pressures[28,29], the dynamic pressure being the 2nd-order term of the asymptotic expansion of the fluid pressure at low Mach numbers.

On the right-hand side of Eq. (2), $\widetilde{\boldsymbol{S}}$ is the filtered strain-rate tensor, $\widetilde{\boldsymbol{S}} = \frac{1}{2}\left(\boldsymbol{\nabla}\widetilde{\boldsymbol{u}} + (\boldsymbol{\nabla}\widetilde{\boldsymbol{u}})^{\top}\right)$, $\mathbf{I}$ the identity matrix, and μ is the dynamic viscosity. In Eq. (3), c_p is the specific heat, λ the thermal conductivity and $p_0(t)$ the 1st-order term of the asymptotic expansion of pressure at low Mach numbers, interpreted as the thermodynamic pressure. According to the low-Mach-number expansion, it is spatially uniform and a function of time only. For open domains, which is the case for this study, p_0 is constant and equal to the ambient pressure. Further, in the governing equations, $\boldsymbol{\tau}^{\mathrm{r}}$ and $\boldsymbol{q}^{\mathrm{r}}$ stand for the sub-grid scale stress tensor and heat flux, respectively.

We add that mass loss due to evaporation is not modelled and consequently the surface level is constant throughout. For the highest evaporation case the mass loss would be equivalent to 3%. This is considered to have a minor effect on the free-surface level, and hence on the aspect ratio and Ra, over the simulation times investigated.

In order to close the system of governing equations, an isobaric "equation of state" for the water density is required. More specifically, a $\overline{\rho} - \widetilde{T}$ relation is introduced. This relation is a fourth-order polynomial fit, see Eq. (4), of tabulated data for water density at the ambient pressure and over the temperature range of interest[30]. The other fluid thermodynamic properties, λ and μ are also calculated from a quartic polynomial fit, with data originating from the same reference. For a generic quantity ϕ, this fit reads

$$\phi = c_4\widetilde{T}^4 + c_3\widetilde{T}^3 + c_2\widetilde{T}^2 + c_1\widetilde{T} + c_0\,. \tag{4}$$

For certain simulations with large ΔT, the dynamic viscosity and the thermal conductivity can vary considerably. Even though the density variations are small, the induced variations in the transport properties of water are non-negligible. On the other hand, c_p variations are negligible and it is taken as a constant, case-dependent, value in all simulations.

For the numerical solution of Eqs. (1)–(3) we employ a second-order accurate time-integration scheme, taking into account the values of the convective and diffusive terms in the current and the two previous time steps. Regarding the spatial discretization, the governing equations are discretised using second-order central difference schemes on a collocated grid system. A flux interpolation technique is used in the spirit of Rhie and Chow[31], to avoid the well-known issue of pressure odd-even decoupling[27,32,33].

For the pressure-velocity coupling a PISO-type projection method is used, similar to the methods proposed by Issa[34] and Oliviera and Issa[35] for constant-density flows. The divergence of the momentum equation is taken and the continuity equation is used as a constraint to formulate the variable-coefficient Poisson equation to be solved for $\overline{p}$. In this low-Mach-number PISO algorithm, the temporal derivative of the density, $\frac{\partial\overline{\rho}}{\partial t}$, emerges on the left-hand side of the Poisson equation which would be zero for the incompressible case.

A. Sub-grid scale modelling

The Large-Eddy-Simulation (LES) approach offers a computationally cheaper alternative to fully resolved Direct Numerical Simulations (DNS). According to it, only the large, energy containing eddies are resolved and the effects of the unresolved scales on the flow are modelled. In Eqs. (2) and (3), the terms that appear after filtering are the sub-grid scale stress tensor and sub-grid scale heat flux, respectively defined as,

$$\boldsymbol{\tau}^{\mathrm{r}} = \overline{\rho}(\widetilde{\boldsymbol{u}\boldsymbol{u}} - \widetilde{\boldsymbol{u}}\widetilde{\boldsymbol{u}})\,, \tag{5}$$

$$\boldsymbol{q}^{\mathrm{r}} = \overline{\rho}\left(\widetilde{\boldsymbol{u}}\widetilde{T} - \widetilde{\boldsymbol{u}T}\right). \tag{6}$$

Many LES studies of thermal convection[12,36–38] have used the eddy-viscosity model of Smagorinsky[39]. Wherein, the influence of the filtered-out eddies are approximated as a viscous contribution on the resolved fields. This leads to,

$$\boldsymbol{\tau}^{\mathrm{r}} - \frac{1}{3}\mathrm{Tr}(\boldsymbol{\tau}^{\mathrm{r}}) = \mu_{\mathrm{t}}\left(2\widetilde{\boldsymbol{S}} - \frac{2}{3}(\boldsymbol{\nabla}\cdot\widetilde{\boldsymbol{u}})\mathbf{I}\right), \tag{7}$$

and

$$\boldsymbol{q}^{\mathrm{r}} = \lambda_{\mathrm{t}}\boldsymbol{\nabla}\widetilde{T}\,. \tag{8}$$

Then, the residual kinetic energy term in Eq. (7), $\frac{1}{3}\mathrm{Tr}(\boldsymbol{\tau}^{\mathrm{r}})$, is incorporated in the pressure term $\overline{p}$ of Eq. (2).

Lilly[40] extended the model, using dimensional analysis, to account for the turbulence owing to buoyancy caused by the temperature gradients of the large-scale flow. The inclusion of a buoyancy production term gives the following relation for the turbulent viscosity,

$$\mu_{\mathrm{t}} = \overline{\rho}C_s^2\Delta^2|\widetilde{\boldsymbol{S}}|\left(1 - \frac{Ri}{Pr_{\mathrm{t}}}\right)^{0.5}, \tag{9}$$

with the Richardson number, Ri, given by

$$Ri = \frac{1}{|\widetilde{\boldsymbol{S}}|^2}\frac{|\boldsymbol{g}|}{\rho_{\mathrm{ref}}}\cdot\boldsymbol{\nabla}\rho\,. \tag{10}$$

In Eq. (9), C_s is the model constant, Δ is the filter (grid) width for which we choose the cube root of the cell volume, $\Delta =$

$(\Delta x \Delta y \Delta z)^{1/3}$, and $|\widetilde{\boldsymbol{S}}|$ is defined as the square root of twice the double inner product of the filtered strain-rate tensor, that is $|\widetilde{\boldsymbol{S}}| = (2\widetilde{\boldsymbol{S}} : \widetilde{\boldsymbol{S}})^{1/2}$. We note that Eq. (9) reduces to the Smagorinsky model for isothermal flows. Further, Eq. (10) is an approximation of the gradient Richardson number, Ri, valid for low-Mach number flows. The numerator in Eq. (10) is equivalent to the square of the buoyancy frequency, presented here in the form familiar to the oceanography community[41], with ρ_{ref} as a reference density.

In our study we employ the Lagrangian dynamic model[42] adapted for variable density flows. As such, the resolved scales are used to compute C_s locally and at each time-step. This model employs the dynamic procedure[43], where the numerator and denominator used to find C_s are averaged over streamlines. This averaging procedure therefore requires the solution of two further transport equations. Any negative viscosity is removed and the correct behaviour of C_s is found near the walls. Indeed, although some clipping is required in our simulations it is always limited to a few percent. Finally, we use the Reynolds analogy ($\lambda_{\mathrm{t}} = \mu_{\mathrm{t}} c_p / Pr_{\mathrm{t}}$) to compute the eddy conductivity. We take Pr_{t}, also present in Eq. (9), as constant and equal to 0.4 as recommended in Eidson[36].

B. Evaporation model

In a previous publication on evaporation-driven thermal convection[2], we investigated different evaporation rates which formed the basis of a temperature gradient assigned as a non-zero Neumann boundary condition at a shear-free upper boundary. Over a series of simulations, the lower (bottom) wall temperature was then iteratively refined until the statistically stationary solution for the time- and area-averaged upper boundary temperature matched the predicted mean value.

In what follows, we present an improved dynamic and inhomogeneous version of this evaporation model. The new algorithm removes the requirement for iterative simulations and results in significant computational savings. The non-zero Neumann thermal boundary condition is calculated at each time-step and is dependent only on the cell temperature nearest the interface and on fixed ambient conditions.

We find both the evaporative ($\dot{q}''_{\mathrm{evap}}$) and convective ($\dot{q}''_{\mathrm{conv}}$) heat losses at the water-side of the interface and use them to apply a non-zero-Neumann thermal boundary condition of the following form,

$$\frac{\partial \widetilde{T}}{\partial y} \; = \; \frac{1}{\lambda_{\mathrm{int}}} \left(\dot{q}''_{\mathrm{conv}} + \dot{q}''_{\mathrm{evap}} \right) \; = \; \frac{1}{\lambda_{\mathrm{int}}} \left(\dot{q}''_{\mathrm{conv}} + \dot{m}'' h_{\mathrm{lv}} \right) , \quad (11)$$

where $\dot{m}''$ is the evaporative mass flux, h_{lv} is the latent heat of evaporation, and $\lambda_{\mathrm{int}} \partial \widetilde{T} / \partial y$ is the heat flux at the water-side of the interface, with λ_{int} as the thermal conductivity of water at T_{int}.

Beginning with the evaporative heat losses, the first step in finding $\dot{m}''$ is to fix the gas-side conditions. Table I provides the temperature (T_∞), ambient pressure (p_0) and relative humidity at a distance far from the interface.

TABLE I. Gaseous mixture properties far from the interface (at ∞). In this table T_∞ is the ambient temperature, p_0 the ambient pressure, RH is the relative humidity, and $p_{\mathrm{v},\infty}$ and ρ_∞ are the water vapour partial pressure and gaseous mixture density far from the interface.

T_∞ (K)	p_0 (Pa)	RH (%)	$p_{\mathrm{v},\infty}$ (Pa)	ρ_∞ ($\frac{\mathrm{kg}}{\mathrm{m}^3}$)
298.15	101325	40	1270	1.18

The water vapour partial pressure, $p_{\mathrm{v},\infty}$, is calculated from a Wagner equation[44] of the following form,

$$p_{\mathrm{v}} \; = \; p_{\mathrm{c}} \exp\Big((a\tau + b\tau^{1.5} + c\tau^3 + d\tau^6)/T_{\mathrm{r}} \Big) , \qquad (12)$$

where p_{c} and T_{c} are respectively the critical pressure and temperature, $T_{\mathrm{r}} = \widetilde{T}/T_{\mathrm{c}}$ is the reduced temperature and $\tau = 1 - T_{\mathrm{r}}$, with the constants available in the literature[45]. The vapour mass fraction far from the interface, $Y_{\mathrm{v},\infty}$, is then found from,

$$Y_{\mathrm{v}} \; = \; \frac{p_{\mathrm{v}} M_{\mathrm{w}}}{p_{\mathrm{v}} M_{\mathrm{w}} + (p_0 - p_{\mathrm{v}}) M_{\mathrm{a}}} , \qquad (13)$$

where M_{w} and M_{a} are respectively the molar masses of water and air. Assuming a binary mixture of water vapour and air, the mass fraction of air far from the interface is then equal to $1 - Y_{\mathrm{v},\infty}$. The gaseous mixture density far from the interface, ρ_∞, is calculated from the ideal-gas equation of state,

$$\rho_{\mathrm{g}} \; = \; \frac{M_{\mathrm{w}} p_{\mathrm{v}}}{RT} + \frac{M_{\mathrm{a}}(p_0 - p_{\mathrm{v}})}{RT} , \qquad (14)$$

where ρ_{g} is the gaseous mixture density, $R = 8314$ J/kmol/K is the universal gas constant and T is the relevant temperature.

Equivalently, we find the conditions *at* the interface; this requires the local T_{int}, from which we find the local properties of saturation pressure, $p_{v,\mathrm{int}}$, the vapour mass fraction, $Y_{\mathrm{v,int}}$, and mixture density, ρ_{int}, all calculated in the same manner as above.

Transition from the interface conditions to those far away is assumed to occur over a layer of finite thickness, or a *film*. Film properties are estimated from mean values of the interface and those at ∞. The quantities ρ_{f} and μ_{f} representing respectively the *film* density and dynamic viscosity are required. This latter quantity is found from the kinetic theory of gases assuming a two-component mixture[46],

$$\mu_{\mathrm{f}} \; = \; \sum_{i=1}^{2} \frac{x_i \mu_i}{x_1 \phi_{i1} + x_2 \phi_{i2}} , \qquad (15)$$

with

$$\phi_{\mathrm{ij}} \; = \; \frac{[1 + (\mu_{\mathrm{i}}/\mu_{\mathrm{j}})^{1/2} (M_{\mathrm{j}}/M_{\mathrm{i}})^{1/4}]^2}{\sqrt{8}[1 + (M_{\mathrm{i}}/M_{\mathrm{j}})]^{1/2}} . \qquad (16)$$

where x_i is the molar fraction of component i and values for air and vapour dynamic viscosities are found from polynomial fits. The film kinematic viscosity, ν_{f} is then inferred from the above quantities. On the other hand, the film mass diffusivity for the binary mixture of air and vapour, D_f, is found from[47],

$$D_\mathrm{f} \;=\; 1.87\times10^{-10}\,\frac{T_\mathrm{f}^{2.072}}{p_0} \qquad \left(\frac{\mathrm{m}^2}{\mathrm{s}}\right), \tag{17}$$

where the thermodynamic pressure, p_0, is in units of atmospheres, i.e. equal to 1 atm. The film diffusion coefficients are used to find the Schmidt number, Sc, and we evaluate the concentration Rayleigh number, Ra_c, as

$$Ra_\mathrm{c} \;=\; \frac{|\boldsymbol{g}|\,(\rho_\infty-\rho_\mathrm{int})\,W^3}{D_\mathrm{f}\mu_\mathrm{f}}\,, \tag{18}$$

with W being the characteristic length-scale, the width of the domain. We use a Sherwood number, Sh, correlation for natural convection flows[17], to find the concentration boundary layer height, δ_c,

$$Sh \;=\; 0.23\,Sc^{0.333}{Ra_\mathrm{c}}^{0.321} \approx \frac{W}{\delta_\mathrm{c}}\,. \tag{19}$$

The mass flux can then be estimated from[48],

$$\dot{m}'' \;=\; \frac{\rho_\mathrm{f}D_\mathrm{f}}{\delta_\mathrm{c}}\log\left(1+B_\mathrm{m}\right), \tag{20}$$

with the mass transfer driving force, B_m, defined as

$$B_\mathrm{m} \;=\; \left(\frac{Y_{\mathrm{v},\infty}-Y_{\mathrm{v,int}}}{Y_{\mathrm{v,int}}-1}\right). \tag{21}$$

Substituting (19) into (20) gives the final mass flux relation,

$$\dot{m}'' \;=\; Sh\frac{\rho_\mathrm{f}D_\mathrm{f}}{W}\log\left(1+B_\mathrm{m}\right). \tag{22}$$

Finally, we find h_lv from a Watson relation[49],

$$h_\mathrm{lv} \;=\; 2256.4\left(\frac{T_\mathrm{c}-T_\mathrm{int}}{T_\mathrm{c}-373.15}\right)^n \tag{23}$$

with the exponent $n = 0.283$.

Next, we concentrate on the convective heat losses away from the free-surface. We estimate this by assuming that heat transfer away from the interface is proportional to the difference between the temperature of the interface, T_int, and the ambient gas-side temperature, T_∞, with the heat transfer coefficient, h, as the proportionality coefficient. Overall we have the following,

$$\dot{q}''_\mathrm{conv} \;=\; h\left(T_\mathrm{int}-T_\infty\right), \tag{24}$$

where h is estimated from the following correlation for a horizontal flat surface, warmer than the ambient air above[50],

$$\frac{h\,W}{\lambda_\mathrm{f}} \;=\; Nu_\mathrm{t} \;=\; 0.54{Ra_\mathrm{t}}^{0.25}. \tag{25}$$

In the above relation we obtain λ_f in an equivalent manner[51] to μ_f from Eq. (15). The film thermal diffusivity, κ_f is again found from aforementioned quantities, and we define Ra_t as the gas-side thermal Rayleigh number,

$$Ra_\mathrm{t} \;=\; \frac{|\boldsymbol{g}|\beta_\infty\,(T_\mathrm{int}-T_\infty)\,W^3}{\kappa_\mathrm{f}\nu_\mathrm{f}}\,. \tag{26}$$

TABLE II. Thermal boundary conditions for the simulations of the cubic ($\Gamma = 1$) domain. In this table, T_low is the fixed lower wall temperature, and $\partial T/\partial y$, T_int and $\dot{m}''$ are respectively the time- and area-averaged temperature gradient, temperature and evaporative mass flux at the upper boundary. For all cases the time- and area-averaged normalised interface temperature, $\langle\hat{\theta}_\mathrm{int}\rangle_{xz} = -0.5$.

Case	Ra	T_low (K)	$\frac{\partial \mathrm{T}}{\partial \mathrm{y}}$ $\left(\frac{\mathrm{K}}{\mathrm{m}}\right)$	T_int (K)	$\dot{m}''$ $\left(\frac{\mathrm{g}}{\mathrm{m}^2\mathrm{s}}\right)$
DNS1	1.2×10^7	320.95	-1555	318.20	0.36
LES1	1.2×10^7	320.95	-1550	318.05	0.36
LES2	3.0×10^7	335.15	-3480	330.15	0.86
LES3	5.2×10^7	345.15	-5670	338.25	1.46
LES4	8.3×10^7	355.15	-8875	345.55	2.36
LES5	1.3×10^8	365.65	-13725	352.95	3.77

Regarding the initial conditions, the water is quiescent and a linear temperature profile from T_low to a first approximation of T_int (from previous simulations[2]) is imposed across the vertical direction. At the first time-step, the temperature gradient at the upper boundary is assumed to be zero, that is $\partial\widetilde{T}/\partial y = 0$, so that the boundary faces have the same value as their cell-centre neighbour. A flowchart for the above algorithm which finds the temperature gradient at the upper boundary for the following time-step, $\left.\frac{\partial\widetilde{T}}{\partial y}\right|^{n+1}$, is provided in Fig. 17 of the Appendix.

The thermal boundary conditions for the simulations in the cubic ($\Gamma = 1$) domain are presented in Table II. The given T_low is fixed, whereas the remaining columns are the values from the statistically stationary solution. For the study of the aspect ratio in Section IV B we use the same T_low as in the highest evaporation case in cubic ($\Gamma = 1$) domain, that is LES5. We then assess the influence, or lack thereof, of the aspect ratio on the other values. The lowest and highest Ra, which are here representative of low and high mass transfer regimes, correspond to temperature drops across the domain of approximately 3 K and 13 K respectively. With this temperature drop occuring over two thermal boundary layers, one can infer the large discrepancy between bulk and interface temperatures at high evaporation rates discussed in the Introduction.

III. NUMERICAL SET-UP

Before elaborating on the numerical set-up we first note that dimensionless variables are denoted with a hat ($\hat{\cdot}$), and provide nondimensionalisation reference values in Tables III and IV. The reference velocity is the free-fall velocity, $U_\mathrm{ff} = \sqrt{|\boldsymbol{g}|H\beta_\mathrm{ref}\Delta T}$, from which the reference free-fall time is found, $t_\mathrm{ff} = H/U_\mathrm{ff}$. Further, the reference temperature, T_ref, is the mean of the lower wall and (time- and area-averaged) interface temperatures, with all reference properties then relative to T_{ref}. With this in mind, the normalised temperature is defined as,

$$\hat{\theta} \;=\; (\widetilde{T} - T_{\text{ref}})/\Delta T\,, \tag{27}$$

and the Rayleigh number, found from the reference values as,

$$Ra \;=\; \frac{g\beta_{\text{ref}}(T_{\text{low}} - T_{\text{int}})H^3}{\nu_{\text{ref}}\kappa_{\text{ref}}}\,. \tag{28}$$

The current configuration differs from a turbulent RBC setup in its upper hydrodynamic and thermal boundary conditions. The lower wall is located at $\hat{y} = 0$, the upper boundary at $\hat{y} = 1$ and, likewise, the side walls at $\hat{x} = 0$ ($\hat{z} = 0$) and $\hat{x} = 1$ ($\hat{z} = 1$). No-slip velocity boundary conditions are enforced at the side and lower walls. The free-slip condition is prescribed at the upper boundary, so that $\frac{\partial \hat{u}}{\partial \hat{y}} = \frac{\partial \hat{w}}{\partial \hat{y}} = 0$ and $\hat{v} = 0$ at $\hat{y} = 1$. This acts as a first order approximation of a free surface. For the thermal boundary conditions we have adiabatic side-walls with $\frac{\partial \hat{\theta}}{\partial \hat{x}}$ prescribed. At $\hat{y} = 0$ we set $\hat{\theta} = 0.5$ as a Dirichlet boundary condition, whereas at $\hat{y} = 1$ we calculate and prescribe at each time step the non-zero Neumann condition explained in detail in Section II B and in the Appendix. For completeness, the statistically stationary dimensionless temperature gradients at the interface for LES1–LES5 are 24.1, 31.3, 37.0, 41.6 and 49.0. Similarly, for the aspect ratio study the equivalent values for LES6 and LES7 are 94.9 and 180.7; the increase being due to the change in the height of the domain.

As a result of the aforementioned boundary conditions, five hydrodynamic boundary layers exist, one at each of the vertical side walls and one at the lower wall. On the other hand, there are only two thermal boundary layers, at the cooled upper boundary and heated lower wall.

A. Resolution criteria

In this section we present the resolution criteria for the fully resolved DNS and the LES. The accuracy of a DNS is ensured only when the smallest length scales of the flow are everywhere resolved. The first criterion is therefore to ensure adequate resolution of the hydrodynamic and thermal boundary layers in the vertical direction. Here, we use the criterion based on the Prandtl-Blasius boundary layer theory[52], which assumes the boundary layers to be laminar at the Ra investigated herein. The number of cells in the hydrodynamic, $N_{\boldsymbol{u}}$, and the thermal, N_θ, boundary layers for all simulations are provided in Table V with the numbers inside the parentheses representing the minimum requirements and those outside the true values. We note that the boundary layers are overresolved by a factor of three for the DNS, whereas only the minimum requirements are met for the LES. We use a hyperbolic tangent expansion function to cluster cells near the walls and expand into the bulk.

The second criterion is the maximum cell size in the bulk of the domain. Here, we assume homogenous isotropic turbulence exists away from the walls and that, for the DNS, all eddies down to the Kolmogorov length-scale, η, must be resolved. In fact, for fluids with $Pr > 1$, which is the case in all simulations investigated here, the temperature microscale, η_θ, is limiting. With respect to the DNS we therefore ensure that all cells are smaller than the *a priori* estimation of the temperature microscale given as follows[53,54],

$$\Delta \;\leqslant\; \pi\eta_\theta \;\approx\; \pi H\left(\frac{1}{Ra\,Pr\,Nu}\right)^{0.25}. \tag{29}$$

Clearly we require an estimation of the global Nusselt number, Nu, for Eq. (29). To this end we first define a local Nusselt number, Nu_y, as the sum of convective, diffusive and turbulent contributions as follows,

$$Nu_y \;=\; \underbrace{\sqrt{RaPr}\,\langle\hat{\rho}\hat{v}\hat{\theta}\rangle_{xz}}_{Nu_{\text{conv}}} \underbrace{-\langle\hat{\lambda}\frac{\partial\hat{\theta}}{\partial\hat{y}}\rangle_{xz}}_{Nu_{\text{diff}}} \underbrace{-\langle\hat{q}^{\text{r}}\rangle_{xz}}_{Nu_{\text{turb}}}, \tag{30}$$

with the turbulent contribution estimated via the dimensionless version of Eq. (8). The global Nusselt is then defined as above except that volume-averaging is carried out, i.e. $\langle..\rangle_{xyz}$. Specifically, for Nu in Eq. (29) we use the relation, $Nu = 0.178Ra^{0.301}$, from a previous publication based on a similar thermal configuration[2].

On the other hand, the maximum cell size in the bulk for the LES is less stringent. The mesh plays the role of the filtering cut-off length, which must be in the inertial subrange. An *a priori* estimation can be found using the Taylor microscale, η_l. For isotropic turbulence this is given[55] by $\eta_l = (15\nu\boldsymbol{u}^{*2}/\varepsilon)^{1/2}$, where $\boldsymbol{u}^*$ is representative of the velocity in the bulk. Here we use the square root of the bulk turbulent kinetic energy given as,

$$\boldsymbol{u}^* = \sqrt{K_{\text{bulk}}} = \sqrt{\frac{(v_{\text{rms}})^2_{\text{bulk}} + (\bar{u}_{\text{rms}})^2_{\text{bulk}}}{2}}\,, \tag{31}$$

with $(v_{\text{rms}})_{\text{bulk}}$ as the rms of vertical velocity fluctuations in the bulk and $(\bar{u}_{\text{rms}})_{\text{bulk}}$ as the rms of the in-plane velocity fluctuations, also found in the bulk. It is noted that the rms of the in-plane velocity fluctuations is defined as

$$\bar{u}_{\text{rms}} \;=\; \sqrt{\langle u'^2 + w'^2\rangle_{xz}}\,. \tag{32}$$

Again from a similar thermal convection configuration[2], we find the relation $(v_{\text{rms}})_{\text{bulk}}H/\kappa = 0.37Ra^{0.454}$. Similarly, for the rms of in-plane velocity fluctuations we find the relation $(\bar{u}_{\text{rms}})_{\text{bulk}}H/\kappa = 0.16Ra^{0.479}$. With appropriate scaling[56] for the dissipation of the turbulent kinetic energy, ε, the following relation can then be used to find the Taylor microscale,

$$\eta_l \;=\; \frac{H\sqrt{15}\hat{\boldsymbol{u}}^*}{[Ra\,(Nu-1))]^{0.5}}\,, \tag{33}$$

with $\hat{\boldsymbol{u}}^*$ given by,

$$\hat{\boldsymbol{u}}^* = \frac{\boldsymbol{u}^* H}{\kappa} \;=\; \sqrt{0.068Ra^{0.91} + 0.012Ra^{0.96}}\,. \tag{34}$$

TABLE III. Nondimensionalisation reference values for the cubic ($\Gamma = 1$) domain. In this table, Ra is increased between simulations via the thermal boundary conditions. The reference length for all cases in the above table is the height of the domain, $H = 0.045$m. The nondimensionalisation reference values for the DNS are not provided as they are equal to those for LES1.

Case	Γ	Ra	$U_{\mathrm{ff}}\left(\frac{\mathrm{m}}{\mathrm{s}}\right)$	ΔT (K)	T_{ref}	$\rho_{\mathrm{ref}}\left(\frac{\mathrm{kg}}{\mathrm{m}^3}\right)$	$\beta_{\mathrm{ref}}\left(\frac{1}{\mathrm{K}}\right)$	$\nu_{\mathrm{ref}}\left(\frac{\mathrm{m}^2}{\mathrm{s}}\right)$	$\kappa_{\mathrm{ref}}\left(\frac{\mathrm{m}^2}{\mathrm{s}}\right)$	Pr_{ref}
LES1	1	1.2×10^{7}	0.023	2.9	319.5	989.6	4.3×10^{-4}	5.84×10^{-7}	1.54×10^{-7}	3.8
LES2	1	3.1×10^{7}	0.034	5.0	332.6	983.5	5.1×10^{-4}	4.76×10^{-7}	1.58×10^{-7}	3.0
LES3	1	5.1×10^{7}	0.041	6.9	341.7	978.6	5.6×10^{-4}	4.20×10^{-7}	1.61×10^{-7}	2.6
LES4	1	8.4×10^{7}	0.051	9.6	350.4	973.5	6.1×10^{-4}	3.75×10^{-7}	1.63×10^{-7}	2.3
LES5	1	1.3×10^{8}	0.060	12.7	359.3	967.9	6.5×10^{-4}	3.40×10^{-7}	1.65×10^{-7}	2.1

TABLE IV. Nondimensionalisation reference values for the study of the aspect ratio. For all cases in this table, T_{low} is the same as that of LES5 (see Table II) and Ra is increased between simulations via the height of the domain. We later assess if the remaining statistically stationary thermal boundary conditions of LES5 persist at the higher Ra (lower aspect ratio).

Case	Ra	Γ	H (m)	$U_{\mathrm{ff}}\left(\frac{\mathrm{m}}{\mathrm{s}}\right)$
LES5	1.3×10^{8}	1	0.045	0.060
LES6	1.1×10^{9}	1/2	0.090	0.086
LES7	8.8×10^{9}	1/4	0.180	0.120

For all LES presented herein, the largest cell size in the bulk is defined as the smallest of either half the Taylor length-scale or a relaxed temperature microscale, taken here as $4\pi\eta_\theta$. Preliminary simulations conducted in the course of this study, showed that this latter relaxed criterion in the bulk serves as a bounding value. We find that meshes with cells of size greater than $4\pi\eta_\theta$ in the bulk, that still satisfy boundary layer requirements for a wall-bounded domain, tend to demand a very large expansion and result in unacceptably high aspect ratios in near-wall cells. We present the final grid resolution criteria in Table V.

In order to assess the DNS refinement *a posteriori* we find the ratios of local grid spacing to the local temperature microscale with this latter quantity defined as follows,

$$\eta_\theta = \left(\kappa^3/\varepsilon\right)^{0.25}, \tag{35}$$

The maximum ratio in the domain is 0.46, as this value is smaller than unity the DNS refinement is considered as adequate. Finally, in all simulations the time-step is calculated from a maximum Courant number of 0.25.

IV. RESULTS

The results section is divided into two parts with the first assessing the validity of both the LES strategy and the evaporation model. In the second part, we decrease the aspect ratio and assess the impact on the LSC state, evaporation rates, mean flow properties and flow statistics. We adopt the following notation: the mean of a generic variable ϕ is denoted by $\langle\phi\rangle$ and refers to time averaging, additional averaging over a given horizontal $x-z$ plane is denoted by $\langle\phi\rangle_{xz}$, and over volume by $\langle\phi\rangle_{xyz}$. The fluctuating component is then denoted by ϕ' and the rms value by $\phi_{\mathrm{rms}} = \sqrt{\langle\phi'\phi'\rangle}$.

Before continuing, we present some global observations by looking at the instantaneous isotherms of an example simulation in Fig. 1. The plumes formed above and below are encouraged into a flow path by the presence of a large-scale circulation in one of the diagonal planes. The same situation is observed whenever the single-roll state is present. Further, we note from Fig. 1 that the minimum normalised temperature in the domain exceeds the lower bound observed in turbulent RBC, that of $\hat{\theta} = -0.5$. This is due to the variable free surface temperature that results in localised cold spots above; the same effect is seen in all cases investigated herein.

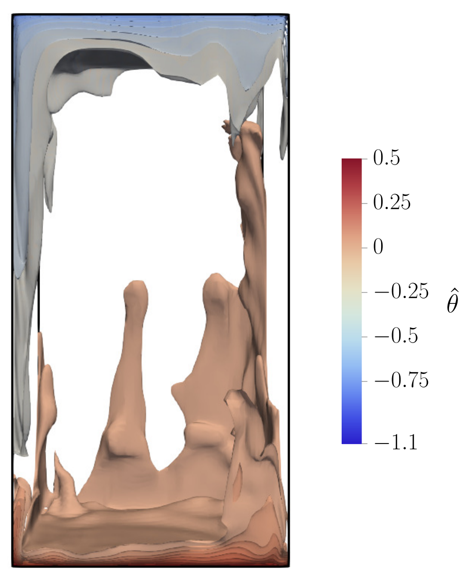

FIG. 1. Example instantaneous isotherms coloured by the normalised temperature, $\hat{\theta}$. The case shown is at aspect ratio $\Gamma = 1/2$ and $Ra = 1.1\times10^{9}$.

TABLE V. Resolution criteria. In this table, N_x, N_z and N_y are respectively the number of cells in the x, z and y directions, $N_{\boldsymbol{u}}$ and N_θ are the number of cells inside the hydrodynamic and thermal boundary layers with numbers in parentheses providing the minimum requirement and those outside the true values. The terms $\hat{\Delta}y_{\text{min}}$ and $\hat{\Delta}y_{\text{max}}$ are respectively the smallest and largest cell size, $\frac{\eta_l}{2}$ is half the Taylor microscale and $4\pi\eta_\theta$ is the relaxed *a priori* temperature microscale prediction. We add for the DNS that $\pi\eta_\theta = 0.017$ so that Eq. (29) is satisfied as $\hat{\Delta}y_{\text{max}} = 0.014$. Finally, t_{avg} is the averaging time for statistics in free-fall time units.

Case	Γ	Ra	$N_x \times N_z$	N_y	$N_{\boldsymbol{u}}$	N_θ	$\hat{\Delta}y_{\text{min}}$	$\hat{\Delta}y_{\text{max}}$	$\frac{\eta_l}{2}$	$4\pi\eta_\theta$	t_{avg}
DNS1	1	1.2×10^7	130×130	130	14 (5)	10 (3)	1.6×10^{-3}	0.014	/	/	300
LES1	1	1.2×10^7	40×40	40	6 (5)	5 (3)	2.4×10^{-3}	0.059	0.059	0.069	300
LES2	1	3.0×10^7	48×48	48	6 (5)	5 (4)	1.9×10^{-3}	0.050	0.052	0.057	300
LES3	1	5.2×10^7	54×54	54	6 (6)	5 (4)	1.6×10^{-3}	0.044	0.044	0.047	300
LES4	1	8.1×10^7	60×60	60	6 (6)	5 (4)	1.5×10^{-3}	0.040	0.041	0.042	300
LES5	1	1.3×10^8	64×64	64	6 (6)	5 (5)	1.4×10^{-3}	0.037	0.037	0.037	400
LES6	1/2	1.1×10^9	64×64	128	8 (8)	6 (6)	6.4×10^{-4}	0.019	0.025	0.019	600
LES7	1/4	8.8×10^9	64×64	256	9 (11)	7 (9)	6.2×10^{-5}	0.009	0.017	0.010	800

TABLE VI. Time-averaged results for cubic ($\Gamma = 1$) domain. In this table, Nu is the global Nusselt number, $\hat{\delta}_{\theta_{\text{int}}}$ and $\hat{\delta}_{\theta_{\text{low}}}$ are the thermal boundary layer heights at the interface and the lower wall respectively, whereas $\hat{\delta}_{\boldsymbol{u}}$ is the hydrodynamic boundary layer height at the lower wall. Finally, we provide the global Reynolds number, Re, defined in the text.

Case	Ra	Nu	$\hat{\delta}_{\theta_{\text{int}}}$	$\hat{\delta}_{\theta_{\text{low}}}$	$\hat{\delta}_{\boldsymbol{u}}$	Re
DNS1	1.2×10^7	24.9	0.014	0.024	0.040	205
LES1	1.2×10^7	24.2	0.015	0.023	0.042	210
LES2	3.0×10^7	31.7	0.011	0.017	0.029	410
LES3	5.1×10^7	36.8	0.0094	0.013	0.028	600
LES4	8.3×10^7	41.7	0.0086	0.011	0.023	840
LES5	1.3×10^8	47.4	0.0074	0.010	0.022	1150

A. Validation

In this section we focus on the the cubic ($\Gamma = 1$) domain and compare flow statistics of the fully resolved DNS against an LES at a moderate $Ra = 1.2\times10^7$. We then compare a series of LES predictions of evaporative mass loss at the free surface against experimental data as a means of testing the accuracy of the implemented evaporation model.

We first compare DNS and LES predictions of the "convective plus turbulent" and diffusive contributions to Nu_{y} in Figs. 2a and 2b respectively. The convective component is the dominant contribution in the bulk but tends to a very small value inside the thermal boundary layers. For the diffusive component, Nu_{diff}, only the near-wall contribution is shown, as it is negligible in the bulk. We observe that the LES underpredicts Nu_{y} everywhere by approximately 3%, which is due to the chosen model and associated resolution. Overall, the 3% underprediction is a satisfactory result for the LES, given the coarseness of the meshes used, which were required for the taking of statistics over long simulations.

For all flows studied herein, a statistically stationary state is achieved when Nu_y is constant along the vertical and further equal to Nu. For all cases investigated, the final Nu differed by a maximum of 1.5% from the Nu found after half the averaging time. The time-averaging interval can therefore be considered adequate.

We now compare the DNS and LES predictions of the rms of velocity fluctuations in Fig. 3. In Fig. 3a we note a near parabolic profile for $\hat{v}_{\text{rms}}$ with zero values at the boundaries. The profiles are similar to those of other thermal convection set-ups with shear-free upper boundary conditions[1,2,12]. The profile is not symmetric with respect to the mid-plane $\hat{y} = 0.5$ as a result of the different strengths in ascending and descending plumes[12], the latter being stronger. We find that the LES predictions are very close to those of the DNS but slightly underpredict the peak in the upper half of the domain.

The $\bar{u}_{\text{rms}}$ profile is presented in Fig. 3b. We observe a unique hydrodynamic boundary layer at the lower wall and a maximum in the rms of in-plane velocity fluctuations found at the surface. This feature has been observed experimentally[10] for evaporative cooling and numerically[2,12] for thermal convection configurations with a shear-free upper boundary. The profile in the bulk of Fig. 3b is different to that seen in similar thermal convection flows with periodic boundaries[12,57] where the bulk profile is flat. This feature of the profile is attributed to the side-wall boundaries leading to counter-rotating vortical cells. For the DNS, the maximum bulk value seen in Fig. 3b corresponds approximately to the vertical position at which the counter-rotating vortical cells interact. The same is true for the LES, however due to the coarseness of the mesh, the peak is less pronounced.

Finally, the hydrodynamic boundary layer created by the shear of the large-scale circulation has a height, $\hat{\delta}_{\boldsymbol{u}}$, estimated from the local peak in $\bar{u}_{\text{rms}}$[57,58]. The LES predicts a boundary layer height very close to that of the DNS, as seen in Table VI, suggesting that the hydrodynamic boundary layer is well-resolved in the LES. We add that we observe in Table VI the expected hydrodynamic boundary layer thinning as Ra is increased.

We next compare the DNS and LES predictions of the mean temperature and rms of temperature fluctuations respectively in Figs. 4a and 4b. Firstly, in Fig. 4a we note that boundary layers exist at both the upper and lower boundaries and that

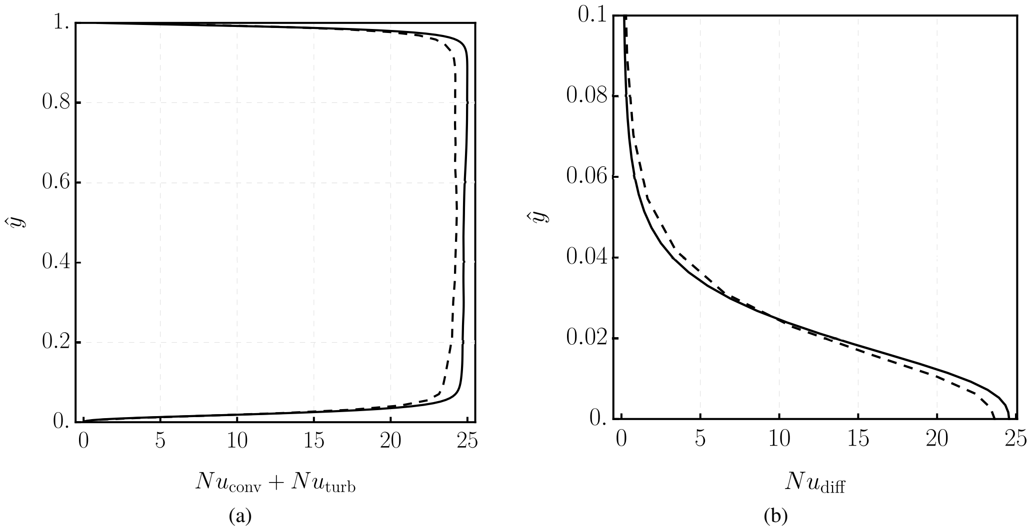

FIG. 2. Plots of the time- and area-averaged components of Nu_y at $Ra = 1.2 \times 10^7$. (a) $Nu_{\mathrm{conv}} + Nu_{\mathrm{turb}}$ across the vertical direction and (b) Nu_{diff} zoom on lower boundary. The legend is as follows: DNS (——), LES (– –).

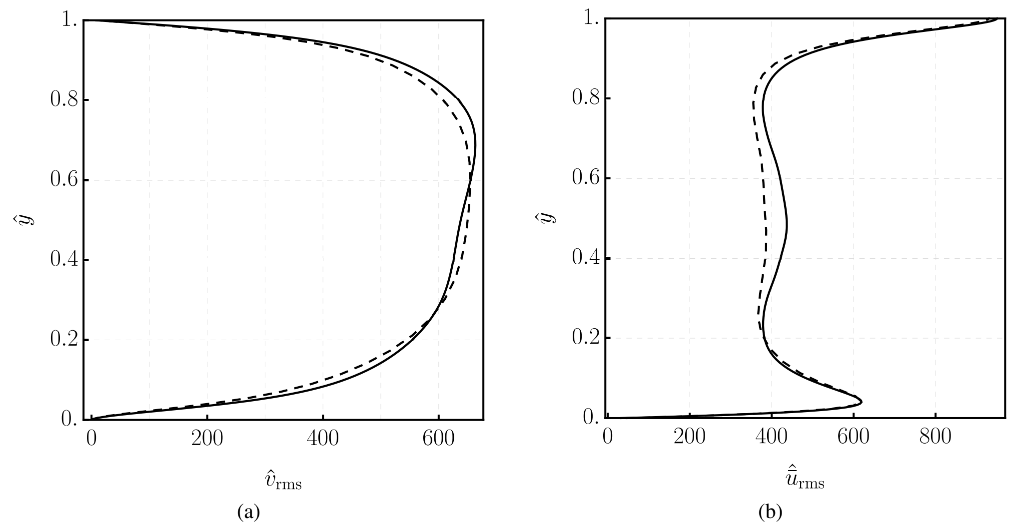

FIG. 3. Plots of the rms of velocity fluctuations at $Ra = 1.2 \times 10^7$. (a) $\hat{v}_{\mathrm{rms}}$ and (b) $\hat{\hat{u}}_{\mathrm{rms}}$. The velocities have been made dimensionless by κ_{ref}/H. The legend is as follows: DNS (——), LES (– –).

the bulk temperature gradient is essentially zero. We further note that the bulk temperature is shifted towards the cooler upper boundary value, as also seen in similar configurations with a shear-free upper boundary[1,2]. This is in contrast to turbulent RBC[57] where the bulk temperature is the mean of the upper and lower boundaries. We present also a zoom on the upper and lower boundaries as insets, where we see that the LES reproduces well the profile. In Fig. 4b we note a local peak near the lower wall representing the location of the thermal boundary layer, $\hat{\delta}_{\theta_{\mathrm{low}}}$, before dropping in the bulk and increasing to a maximum at the upper boundary. We again show insets which suggest that the LES reproduces well the DNS results. In particular we note that the height of the lower thermal boundary layer appears well predicted. The upper thermal boundary layer height, $\hat{\delta}_{\theta_{\mathrm{int}}}$, on the other hand is estimated as follows,

$$\delta_{\theta_{\mathrm{int}}} = -\lambda_{\mathrm{int}} \frac{T_{\mathrm{int}} - T_{\mathrm{bulk}}}{\dot{q}''}, \tag{36}$$

with T_{int} and $\dot{q}''$ respectively as the time- and area-averaged temperature and heat flux at the interface and where the dimensional T_{bulk} is interpreted from Fig. 4a. Table VI confirms that the LES reproduces well the DNS predictions of both $\hat{\delta}_{\theta_{\mathrm{low}}}$ and $\delta_{\theta_{\mathrm{int}}}$, suggesting that the thermal boundary layers are well-resolved in the LES.

We note that $\hat{\delta}_{\theta_{\mathrm{low}}}$ is larger than $\hat{\delta}_{\theta_{\mathrm{int}}}$ and attribute the inhomogeneity to the presence of the shear-free upper boundary[1,2]. This feature of the flow remains even with the non-uniform interface temperature (see later Fig. 12), and indeed temperature gradient at the interface, investigated herein. We add that Table VI shows boundary layer thinning as a result of increasing Ra in the cubic ($\Gamma = 1$) domain, however, the inhomogeneities in the thermal boundary layer heights remain.

Finally, we compare the predictions of the third order statistics of the DNS and LES in Fig. 5. The profile of the third central moment of the temperature is provided as Fig. 5a where we again see an asymmetry introduced by the shear-free upper boundary. The normalised third central moment, the temperature skewness, is defined as $\hat{S}_\theta = \langle \hat{\theta}'^3 \rangle_{xz} / \hat{\theta}^3_{\mathrm{rms}}$. Fig. 5b shows that the temperature is predominantly negatively skewed owing to the more intense plume formation at the shear-free surface[12]. We can see in both aforementioned figures that the third-order statistics are well approximated by the LES, although the peaks are underestimated near the boundaries and, in particular, the LES exaggerates the negative skewness in the upper half of the domain. An increased resolution in the y-direction would lead to the resolution of smaller scales and better predictions in the upper half. Overall, however, we find that the LES predictions of first, second and third order statistics compare satisfactorily with the DNS data.

We next present the validation exercise for the evaporation model, where we start by discussing the experimental setup[14] in the Institut de Radioprotection et de Sûreté Nucléaire (IRSN) of France. The experiments were conducted using a set of insulated stainless steel tanks of differing shapes (cylindrical and cuboidal) and aspect ratios. During the tests, the tanks were filled with water and heated from below. The water mass and free-surface temperatures were then measured simultaneously, the latter using an infrared camera. The ambient gaseous conditions, i.e. the relative humidity and temperature, were also recorded above the experimental device.

Importantly, the tanks were heated up towards, but never arriving at boiling point, so as to avoid initiating any nucleation. At which point the heating was stopped and the water allowed to cool. During both the heat-up and cool-down stages the following parameters were measured: the mass of water in the tank, the bulk water temperature, the interface temperature T_{int}, the ambient air temperature T_∞, and the relative humidity. The collated data allowed for a plot of evaporative mass flux against free-surface temperature with error bars representative of the measurement device accuracy. In Fig. 6, we replot this data and superimpose the time- and area-averaged evaporative mass flux predictions for cases LES1–LES5. We observe that the predicted evaporative mass fluxes are an excellent fit with the best estimate from the experimental measurements and are easily within the limits of experimental error indicated by the shaded grey area. We can therefore assume that the evaporation model is valid.

It is worth noting that discrepancies in experimental results due to variable ambient conditions, tank geometry and the stage of heat transfer (i.e. heat-up or cool-down) were smaller than the margin of errors in the experimental measurement devices. This suggests that the aspect ratio should not play an important role in the rate of evaporation, a result which we confirm in the next section.

Finally, Table VI shows the global Reynolds number, $Re = (\boldsymbol{u}_{\mathrm{rms}})_{\mathrm{xyz}} H/\nu$ where $(\boldsymbol{u}_{\mathrm{rms}})_{\mathrm{xyz}} = \sqrt{\langle u'^2 + v'^2 + w'^2 \rangle}_{\mathrm{xyz}}$ (m/s) is the time- and volume-averaged rms of the velocity fluctuations. Using this data, we obtain the power-law fit over the parameter space as, $Re = 2.7 \times 10^{-3} Ra^{0.69}$. We note that, for the cubic domain, Ra is updated between simulations via the thermal boundary conditions. Consequently, there are large variations in T_{ref} and hence in the kinematic viscosity, ν, between the cases. For this reason, we also provide a power-law fit of the the time- and volume-averaged rms of the velocity fluctuations, as $(\boldsymbol{u}_{\mathrm{rms}})_{\mathrm{xyz}} \propto Ra^{0.47}$. This latter fit of the dimensional rms velocity, matches well that of Scheel and Schumacher[59] for turbulent RBC at $Pr = 0.7$ in cylindrical domains of aspect ratio $\Gamma = 1$, according to which Re scales as Ra^β, with $\beta = 0.49 \pm 0.01$.

B. Study of the effect of the aspect ratio

The purpose of this section is to investigate the role of aspect ratio on the structure of the LSC, evaporation rates, mean flow properties and flow statistics. In relation to the latter, the common technique of increasing Ra in turbulent RBC experiments is to maintain both T_{av} and Γ and increase Ra via thermal boundary conditions, specifically ΔT. In this section however, we maintain the thermal boundary conditions and Ra is updated between simulations by reducing the aspect ratio Γ via the height of the domain.

We start by presenting the time-averaged LSC flow structure in the cubic ($\Gamma = 1$) domain at $Ra = 1.3 \times 10^8$ in Figs. 7 and 8. The streamlines of Fig. 7 suggest a steady single-roll state of the LSC that occupies the entirety of the domain. From Fig. 7a we note that the impingement point of the LSC is aligned in one corner, with the lower wall impingement point (not shown) found in the opposite corner. This is characteristic of a steady LSC in cubic geometries where the single-roll state dominates[2,21]. The same global observations of the LSC are made in all $\Gamma = 1$ simulations. Further, asymmetries are observed in both the recirculation zones of Fig. 8a and in the counter-rotating vortices of Fig. 8b. These are a result of the free-slip upper boundary condition accelerating fluid following impingement[2].

We next present the LSC structure in the domain of aspect ratio $\Gamma = 1/2$ at $Ra = 1.1 \times 10^9$, in Figs. 9 and 10. The same single-roll LSC state exists as seen in the $\Gamma = 1$ case (shown in Figs. 7 and 8); this LSC structure remained unchanged during the simulation. Further, the asymmetries in recirculation zones and counter rotating vortices persist in Figs. 10a and 10b respectively. As discussed in the Introduction, the transition from a single to a dual-roll state is dependent on Ra, Pr and Γ. A $Ra - Pr$ phase diagram was previously proposed[19] for determining whether the mean flow structure is a single or dual-roll states in cylindrical domains of aspect ratio $\Gamma = 1/2$. For the parameter space investigated here, that is $Ra \approx 10^9$ and $Pr \approx 2$, the phase diagram[19] predicts a single-roll state like that observed in Fig. 10a. This result suggests that the experimental studies of the role of aspect ratio on the LSC state in cylindrical domains could also be relevant for cuboidal ap-

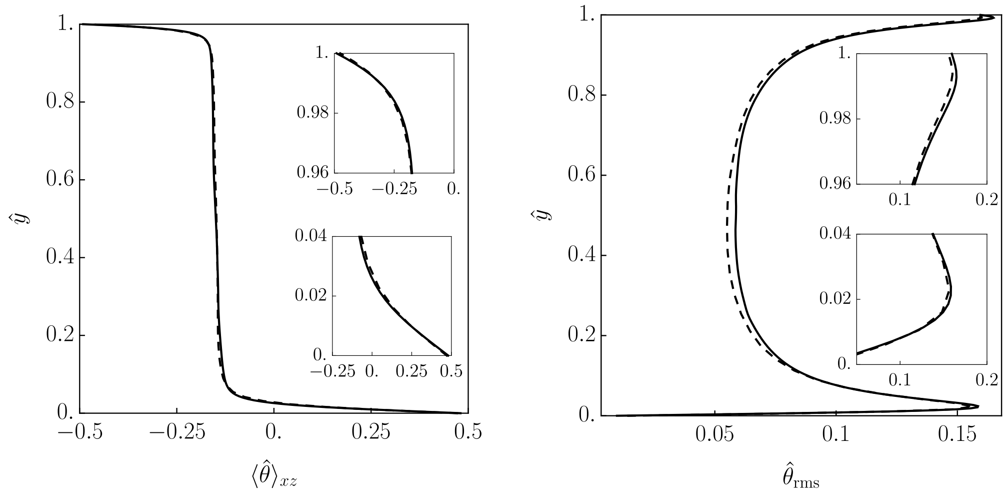

(a) (b)

FIG. 4. Plots of the temperature at $Ra = 1.2 \times 10^7$. (a) Mean, $\langle\hat{\theta}\rangle_{xz}$, and (b) rms, $\hat{\theta}_{\rm rms}$. The legend is as follows: DNS (——), LES (– –).

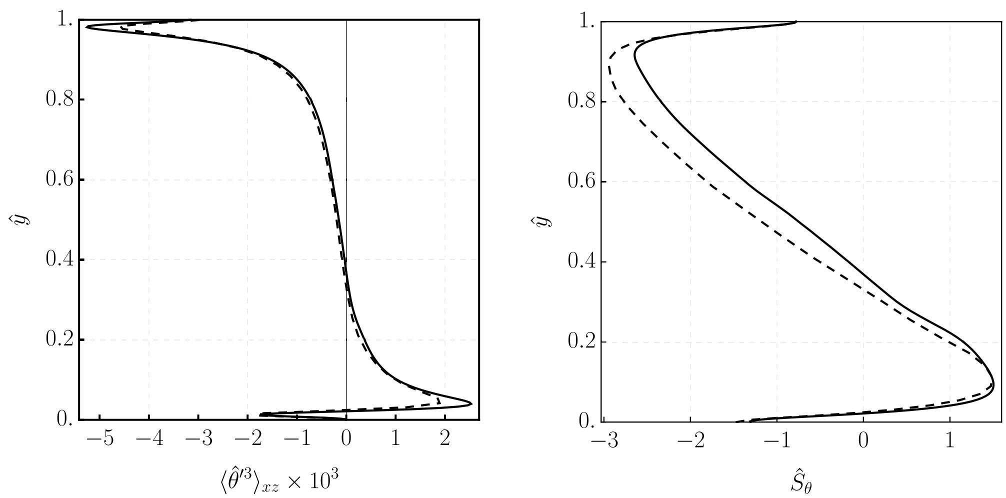

(a) (b)

FIG. 5. Plots of third-order statistics at $Ra = 1.2 \times 10^7$. (a) Third central moment of temperature and (b) Skewness of temperature. The legend is as follows: DNS (——), LES (– –).

plications.

A long lifetime dual-roll state has previously been inferred (but not observed) in a cylindrical domain of aspect ratio $\Gamma = 1/2$ with water as the convecting fluid[60]. However, this observation was later questioned by Weiss and Ahlers [24] who investigated a similar set-up. Therein, it was found that the dual-roll state existed only as a transitional state between re-orientation events of the single-roll LSC (such as drifting, cessations, or torsional oscillations), and as such for very short lifetimes. Their research was again based on a slender cylindrical domain, but the same conclusion can be inferred from Fig. 10 for the cuboidal domain where we see a steady single-roll LSC state.

In Figs. 11a and 11b we present the time-averaged streamlines in the domain of aspect ratio $\Gamma = 1/4$ at $Ra = 8.8 \times 10^9$. In terms of the flow structure we see that the LSC is in a dual-roll state. Such a dual-roll or transitional state is expected to be dominant in low aspect ratio (slender) domains[22]. However, to the authors knowledge, no experimental observations are available in the literature for comparison at the aspect ratio $\Gamma = 1/4$, be that in cylindrical domains or otherwise.

In Fig. 11c, as they are symmetric, we show both diagonal planes together on the same axes, and again superimpose the large-scale structures. These symmetric flow-structures in the dual-roll LSC state are similar to those seen in the orthogonal plane of the single-roll state. As such, the definitions of diagonal planes as LSC and orthogonal, are not appropriate for the dual-roll state.

Regarding the simulation of the domain of aspect ratio $\Gamma = 1/4$, the impingement point above is no longer aligned with a corner, as was the case in Figs. 7a and 9a, but in the centre of the surface, similar to observations made in another aspect

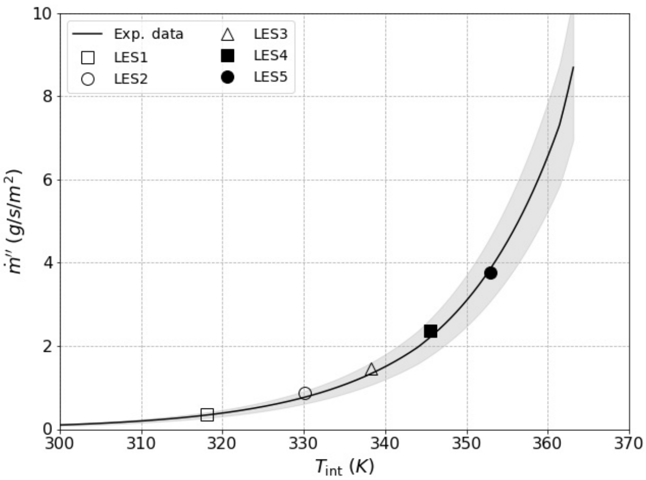

FIG. 6. LES predictions and experimental measurements of the evaporative mass flux, $\dot{m}''$, and interface temperature, $T_{\rm int}$, at an evaporating air-water interface. The shaded area represents the accumulated experimental error ($\sim \pm 20\%$ of the measured flux). All experimental runs, regardless of the ambient conditions or tank geometry lie within the shaded area. The solid line represents a best estimate from all experimental data.

ratio study[61].

Theoretically, reorientation events of the dual-roll LSC are possible during the averaging time of the aspect ratio $\Gamma = 1/4$ simulation. Indeed, such events become more likely as Γ is reduced[25] and the LSC becomes less stable. Unlike in Figs. 8a and 10a, where reorientation events are absent, it is possible that Figs. 11a and 11b represent a time-averaged flow in which reorientation events have occurred. However, we note that the observed flow structure in Fig. 11c appears to remain steady throughout.

We next discuss whether the aspect ratio has an influence on the free surface parameters, and notably on the evaporative mass flux. We first present Fig. 12 showing the mean normalised temperature at the interface, where we observe that $\langle \hat{\theta} \rangle$ varies in space. There is a clear role of the LSC in determining this spatial variation. As the LSC is driven by the hot buoyant plumes released from the lower wall, the warmest locations on the free surface coincide with the impingement point of the LSC.

Remarkably, however, Table VII shows that the time- and area-averaged interface temperature remain steady as *Ra* is increased by almost two orders of magnitude. Consequently, the evaporative mass flux at the free-surface also remains steady and can be considered independent of the water-side *Ra*. At the same time, the reduction in aspect ratio to $\Gamma = 1/4$ and subsequent transformation of the LSC to a non-single-roll state clearly changes the velocity field on the interface; see Fig. 12c. The LSC state therefore also has a negligable influence on the evaporation rate at the interface. These results are in fact in accordance with experimental observations[14] where the geometry of the tanks, that is surface shape and crucially aspect ratio, had no determinable influence on evaporation rates when experimental error was taken into account.

TABLE VII. Thermal boundary conditions for the study of the aspect ratio. In this table, $T_{\rm low}$ is the fixed lower wall temperature, and $\partial T/\partial y$, $T_{\rm int}$ and $\dot{m}''$ are respectively the time- and area-averaged temperature gradient, temperature and evaporative mass flux at the upper boundary taken from the statistically stationary solution. For all cases the time- and area-averaged normalised interface temperature, $\langle \hat{\theta}_{\rm int} \rangle_{xz} = -0.5$.

Case	Γ	*Ra*	$T_{\rm low}$ (K)	$\frac{\partial T}{\partial y}$ $\left(\frac{K}{m}\right)$	$T_{\rm int}$ (K)	$\dot{m}''$ $\left(\frac{g}{m^2 s}\right)$
LES5	1	1.3×10^8	365.65	-13700	352.95	3.77
LES6	1/2	1.1×10^9	365.65	-13600	352.65	3.73
LES7	1/4	8.8×10^9	365.65	-13250	352.35	3.63

TABLE VIII. Time-averaged results for the study of the aspect ratio. In this table, *Nu* is the global Nusselt number, $\hat{\delta}_{\theta_{\rm int}}$ and $\hat{\delta}_{\theta_{\rm low}}$ are the thermal boundary layer heights at the interface and the lower wall respectively, whereas $\hat{\delta}_{\boldsymbol{u}}$ is the hydrodynamic boundary layer height at the lower wall. Finally, we provide the global Reynolds number, *Re*, defined in the text.

Case	Γ	*Ra*	*Nu*	$\hat{\delta}_{\theta_{\rm int}}$	$\hat{\delta}_{\theta_{\rm low}}$	$\hat{\delta}_{\boldsymbol{u}}$	*Re*
LES5	1	1.3×10^8	47.4	0.0074	0.010	0.022	1150
LES6	1/2	1.1×10^9	92.4	0.0036	0.0059	0.012	2555
LES7	1/4	8.8×10^9	172.5	0.0022	0.0026	0.008	5265

With respect to any eventual influence of the aspect ratio on the mean flow properties we assess the dimensionless heat transfer. We start by presenting Fig. 13, where we plot the profiles of the different contributions of Nu_y. The statistically stationary nature of the simulations at aspect ratios $\Gamma = 1$ and $1/2$ is again inferred from the flat profile of $Nu_{\rm conv} + Nu_{\rm turb}$ across the domain in Fig. 13a. However, we note that ideally we would have taken more statistics for the aspect ratio $\Gamma = 1/4$ simulation. We monitored the statistics throughout and confirm that the profile flattens with time. This suggests that if the simulations were carried out over many hundreds more free-fall times the simulation would be fully statistically stationary. Table V shows that we ran this simulation for 800 $t_{\rm ff}$ which is already longer than the vast majority of earlier studies, with the notable exception of Foroozani *et al.* [20,21] who specifically looked at LSC dynamics over long time periods. The global Nusselt, however, varies only by 1.5% if half the averaging time, that is $400 t_{\rm ff}$, is used. This result suggests that *Nu* is representative of a statistically stationary value.

We now present a *Ra*–*Nu* scaling analysis covering a parameter space of nearly 3 decades of *Ra*. This analysis is based on all seven LES, it therefore includes simulations of variable $T_{\rm av}$ and Γ which is only permitted as the *Nu* dependency on *Pr* and aspect ratio is essentially absent[24]. This is certainly true for water at $Pr = 2$, where the thermal boundary layer is sheltered within the hydrodynamic one. Any eventual impact on thermal boundary layer thicknesses as a result of a transition in LSC flow state is then buffered[62]. We obtain the

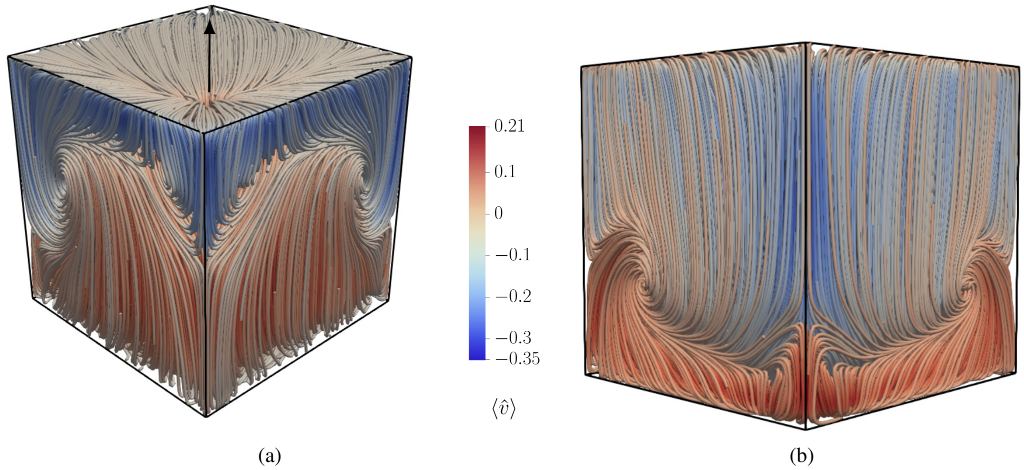

FIG. 7. Time-averaged streamlines in the aspect ratio $\Gamma = 1$ domain at $Ra = 1.2 \times 10^8$, coloured by mean vertical velocity, $\langle \hat{v} \rangle$. (a) Top-view from the front, with the arrow indicating the single-roll LSC plane and direction and (b) side-view from the back.

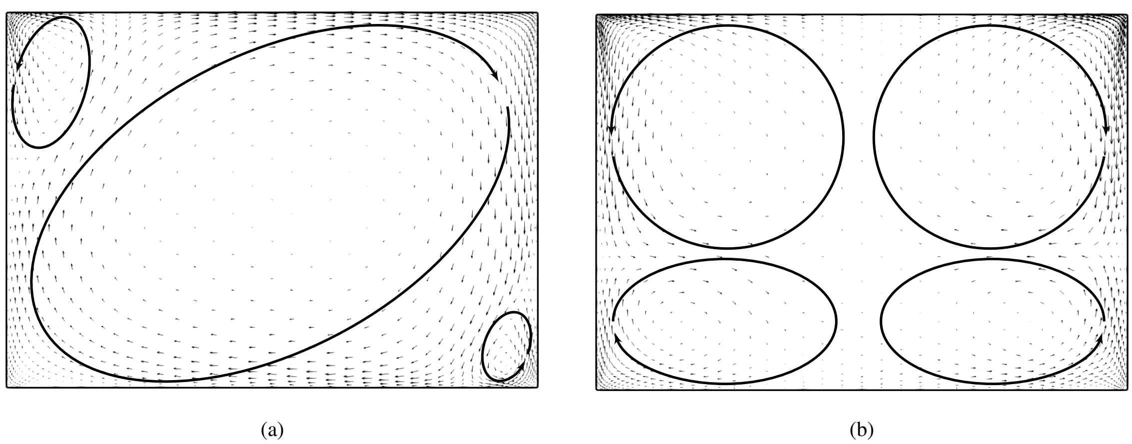

FIG. 8. Time-averaged velocity vectors scaled by magnitude with superimposed large-scale structures in the cubic ($\Gamma = 1$) domain (a) LSC plane, as indicated by the arrow in Fig. 7a and (b) the orthogonal plane. The same global LSC structure is seen across all simulations in the cubic domain.

following power-law fit,

$$Nu = 0.170 Ra^{0.302}, \tag{37}$$

which is remarkably close to the scaling obtained from previous DNS studies in a similar thermal convection configuration[2], which gave $Nu = 0.178 Ra^{0.301}$ over a smaller parameter space. The reduced prefactor here corresponds to the slight underestimation of the LES discussed earlier and the exponent in Eq. (37) is in good agreement with experimental turbulent RBC studies[63] which give $Nu \propto Ra^{0.309}$.

Verzicco[64] looked at turbulent RBC between two free boundaries and two rigid walls. Therein, it was found that heat transfer in the flow between free-slip boundary conditions was twice as large as that of the analogous flow with no-slip velocity boundary conditions. Nevertheless, the power-law fit gave the same exponent, that is $Nu \propto Ra^{0.3}$. Using this information, and taking the prefactor from Niemala *et al.*[63] as ~ 0.12, we can estimate a prefactor of ~ 0.24 for the case of turbulent RBC between two free boundaries. Fig. 14 then shows that (37) fits well within these correlations, with the prefactor being about half as large again as that of Niemala *et al.*[63].

We also provide the relevant global Re in Table VIII. For the study of the effect of the aspect ratio, we update Ra via the height of the domain and, as discussed, the thermal boundary conditions remained almost constant. A power-law fit over the aspect ratio range gives $Re \propto \left(\frac{1}{\Gamma}\right)^{1.07}$; suggesting that the turbulence intensity increases almost linearly with aspect ratio.

We now assess the influence of the aspect ratio on the flow statistics and start by presenting the rms of vertical and in-plane velocity fluctuations in Fig. 15. We first concentrate on the rms of vertical velocity fluctuations, $\hat{v}_{\mathrm{rms}}$, where Fig. 15a shows that the near-parabolic profile observed in Fig. 3a persists in all simulations. In Fig. 15b, we again observe approximately the same trend over all Ra investigated; a peak by the lower wall represents a hydrodynamic boundary layer, the bulk $\bar{u}_{\mathrm{rms}}$ profile shows a bump owing to the contained nature of the flow and a maximum is found at the upper boundary.

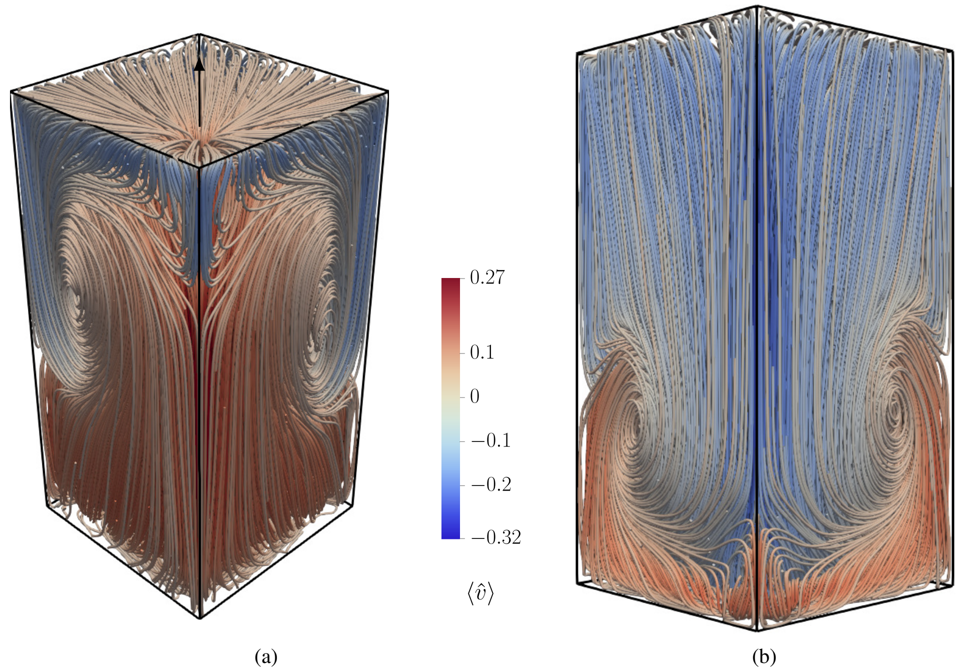

FIG. 9. Time-averaged streamlines in the domain of aspect ratio $\Gamma = 1/2$ at $Ra = 1.1 \times 10^9$, coloured by mean vertical velocity, $\langle \hat{v} \rangle$. (a) Top-view from the front, with the arrow indicating the single-roll LSC plane and direction and (b) side-view from the back.

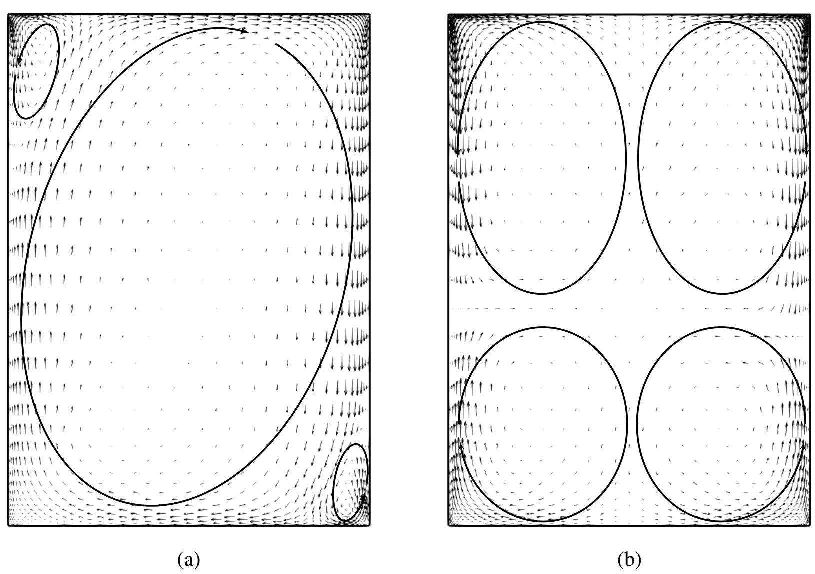

FIG. 10. Time-averaged velocity vectors scaled by magnitude with superimposed large-scale structures for aspect ratio $\Gamma = 1/2$ (a) LSC plane, as indicated by the arrow in Fig. 9a and (b) the orthogonal plane.

Overall, we conclude that the influence of the aspect ratio is limited, as we see the same global trends that would otherwise be observed if the standard manner of increasing *Ra* had been used. That is, the rms of velocity fluctuatations are positively correlated with *Ra*, Table VIII shows thinning of the hydrodynamic boundary layer with *Ra* and the same global profiles are maintained in $\hat{v}_{\mathrm{rms}}$ and $\bar{u}_{\mathrm{rms}}$.

We next discuss the time- and area-averaged normalised temperature distribution in the domain as the aspect ratio is decreased. Fig. 16a suggests a subtle difference between the cases at aspect ratios $\Gamma = 1$ and $\Gamma = 1/2$ where the single-roll state is present and the case at aspect ratio $\Gamma = 1/4$, where the dual-roll dominates. In the current thermal configuration, the temperature in the bulk is expected to be constant and equal to a value shifted towards the cold upper boundary temperature[1,2]. This is indeed the case for aspect ratios $\Gamma = 1$ and $\Gamma = 1/2$. However, for the case at aspect ratio $\Gamma = 1/4$, Fig. 16a clearly shows that outside of the bound-

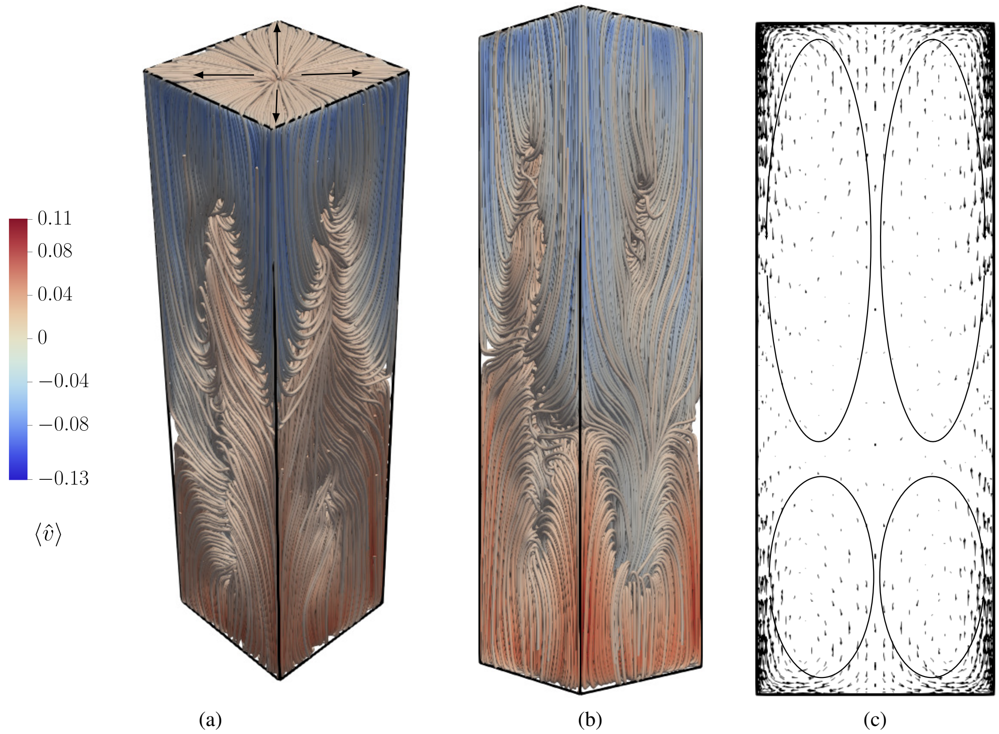

FIG. 11. Time-averaged flow structure in the domain of aspect ratio $\Gamma = 1/4$ at $Ra = 8.8 \times 10^9$ where a dual-roll LSC state is present. (a) Top-view from the front of streamlines coloured by mean vertical velocity, $\langle \hat{v} \rangle$. At the free surface, we see the upper part of the dual-roll LSC, where a central impingement point is observed, (b) same as in (a) but a side-view from the back is shown and (c) velocity vectors scaled by magnitude with superimposed large-scale structures. As the diagonal planes of the dual-roll LSC are now symmetric, we show them together and on the same axes. The diagonal planes then have a similar structure as the orthogonal planes in Figs. 8b and 10b.

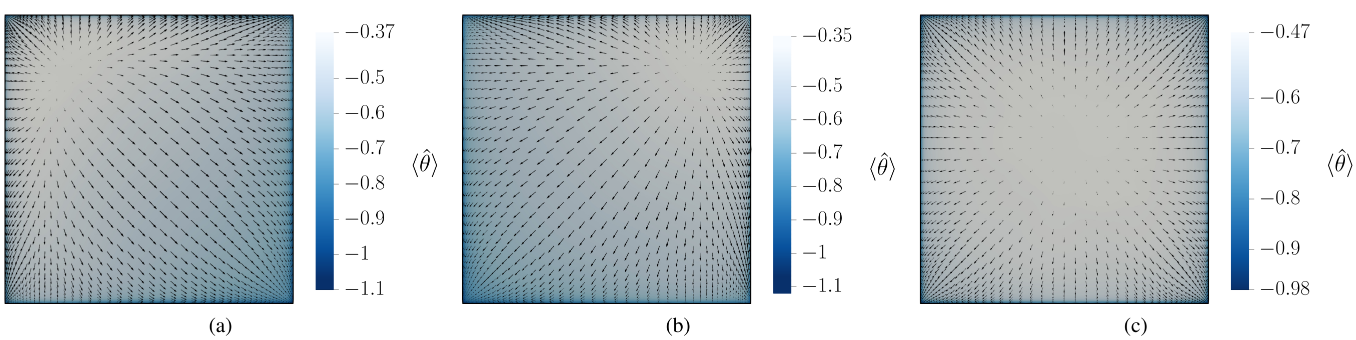

FIG. 12. Time-averaged normalised interface temperatures, $\langle \hat{\theta} \rangle$ with time-averaged velocity vectors scaled by magnitude. (a) Aspect ratio $\Gamma = 1$ at $Ra = 1.2 \times 10^8$, (b) aspect ratio $\Gamma = 1/2$ at $Ra = 1.1 \times 10^9$ and (c) aspect ratio $\Gamma = 1/4$ at $Ra = 8.8 \times 10^9$.

ary layers, the bulk temperature is not constant but in fact increases linearly. Consequently, the bulk temperature is, in general, warmer than for the larger aspect ratio cases. We note that the trend is unchanged if we take only the first half of the averaging time, 400 t_{ff}, and consequently we do not put this feature of the flow down to lack of statistics. Indeed, a peak in bulk fluid temperature as a result of a transition to the dual-roll state has been reported before[65]. Therein, the flow feature was described as being caused by the bringing into contact of the fluid transported from the hot and cold plates in the cell centre, albeit for a fluid at $Pr < 1$ and in a cylindrical domain of aspect ratio $\Gamma = 1/2$. On the basis of our findings, we conclude that the observed bulk temperature gradient is the same effect played out in the cuboidal domain of aspect ratio $\Gamma = 1/4$.

Concentrating next on Fig. 16b, we observe the same general trends as seen in Fig. 4b. That is, a peak at the lower boundary which defines the lower thermal boundary layer height, a dip in the centre of the domain and a maximum at the upper boundary. As Ra is increased the dimensionless thermal boundary layer heights are decreased as seen in Table VIII. The dip in the bulk is reduced, albeit less than one might expect for the largest Ra (smallest Γ), and the maximum at the surface is nearly constant. This result appears to answer

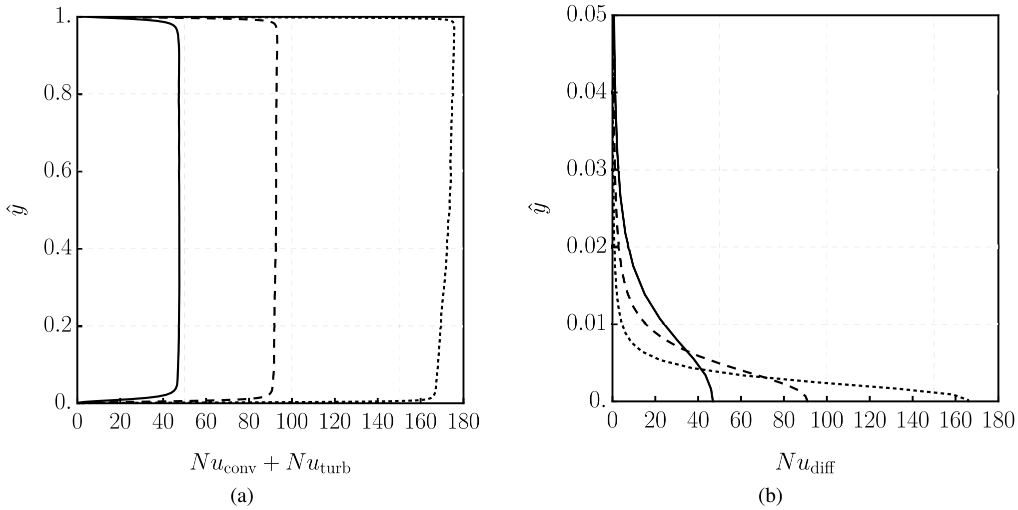

FIG. 13. Plots of the time- and area-averaged components of Nu_y as Ra is increased (Γ is decreased). (a) $Nu_{\mathrm{conv}} + Nu_{\mathrm{turb}}$ across the vertical direction and (b) Nu_{diff} zoom on lower boundary. The legend is as follows: aspect ratio $\Gamma = 1$ at $Ra = 1.3 \times 10^8$ (——), aspect ratio $\Gamma = 1/2$ at $Ra = 1.1 \times 10^9$ (– –) and aspect ratio $\Gamma = 1/4$ at $Ra = 8.8 \times 10^9$ (⋯⋯).

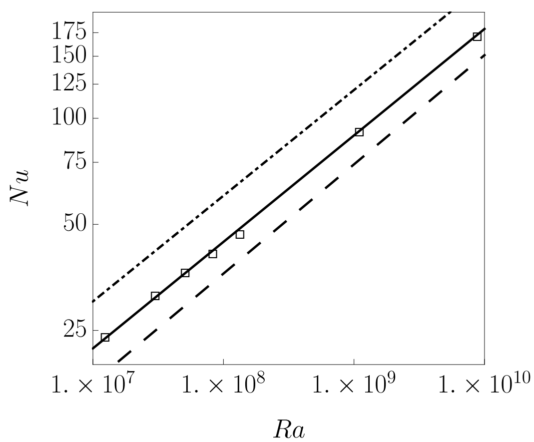

FIG. 14. Ra scaling of Nu. The legend is as follows: Nu data (□), power-law fit to the present data: $Nu = 0.17Ra^{0.302}$ (——), power-law fit of RBC between two rigid boundaries[63]: $Nu = 0.12Ra^{0.31}$ (– –), and power-law fit of RBC between two free boundaries[64]: $Nu = 0.24Ra^{0.30}$ (-·-·). The prefactors have been rounded to two significant figures.

the question posed by Bower and Saylor [17] of whether water-side natural convection can affect evaporation rates. Therein, it was hypothesised that a higher Ra would result in increased $\hat{\theta}_{\mathrm{rms}}$ at the interface. This feature is not observed in Fig. 16b, which shows a constant interface value as Ra is increased. The same cannot be said for the rms of velocity fluctuations which increase significantly at the free surface with Ra, as shown in Fig. 15.

In any case, Table VIII provides values for $\hat{\delta}_{\theta_{\mathrm{int}}}$ where there is visible upper thermal boundary layer thinning as a result of increasing Ra. This is further observed in the inset of Fig. 16a. However, it is of interest here to analyse the *dimensional* upper thermal boundary layer height as Ra is increased. With the interface (see Table VII) and bulk (see Fig. 16a) temperatures approximately constant, all quantities on the RHS of Eq. (36) remain unchanged with Ra, and hence $\delta_{\theta_{\mathrm{int}}}$ is also. If the thermal boundary layer on the water-side of the air-water interface remains the same thickness, then heat and mass transfer at the interface should indeed be controlled by the air-side conditions as is the case here.

V. CONCLUSION

We have presented and validated an algorithm for predicting evaporation rates at an air-water interface. Over a series of LES the algorithm and simulation strategy are shown to accurately reproduce the experimental measurements of evaporative mass flux and interface temperatures. We then fixed the thermal boundary condition at the lower wall and show that the aspect ratio and water-side turbulence play no measurable role on the evaporation rate above.

Over a series of simulations the aspect ratio is shown to influence the LSC, which changes from a steady single-roll state to a dual-roll equivalent. It appears that many of the observations on the influence of the aspect ratio on the state of the large-scale circulation, originally made in cylindrical containers, are in fact applicable to cuboidal domains. That is, the likelihood of the single-roll state diminishes greatly in low aspect ratio domains and is dominant in domains of aspect ratio $\Gamma = 1$ and $1/2$. However, we observe that the eventual transition to a dual-roll state at low aspect ratio had no determinable impact on the heat transfer within the domain and hence on the evaporation rates above, at least within the accuracy of the LES carried out.

In future work we intend to take into account the descending interface, and hence the dynamic calculation of Ra and aspect ratio. This will allow for longer simulation times at higher evaporation rates in order to assess the LSC dynamics.

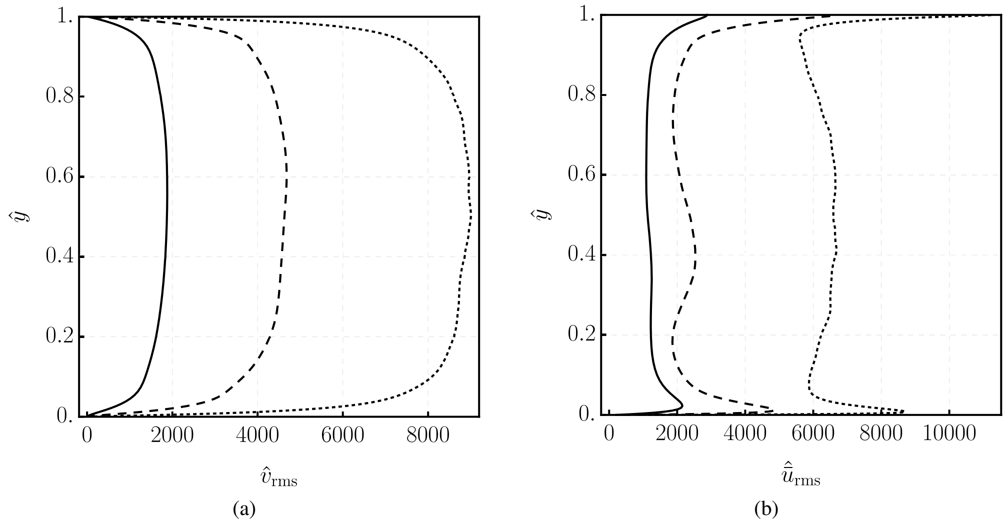

FIG. 15. Plots of the rms of velocity fluctuations as Ra is increased (Γ is decreased). (a) $\hat{v}_{\rm rms}$ and (b) $\hat{u}_{\rm rms}$. The velocities have been made dimensionless by $\kappa_{\rm ref}/H$ and the legend is as follows: aspect ratio $\Gamma = 1$ at $Ra = 1.3 \times 10^8$ (——), aspect ratio $\Gamma = 1/2$ at $Ra = 1.1 \times 10^9$ (— —) and aspect ratio $\Gamma = 1/4$ at $Ra = 8.8 \times 10^9$ (⋯⋯).

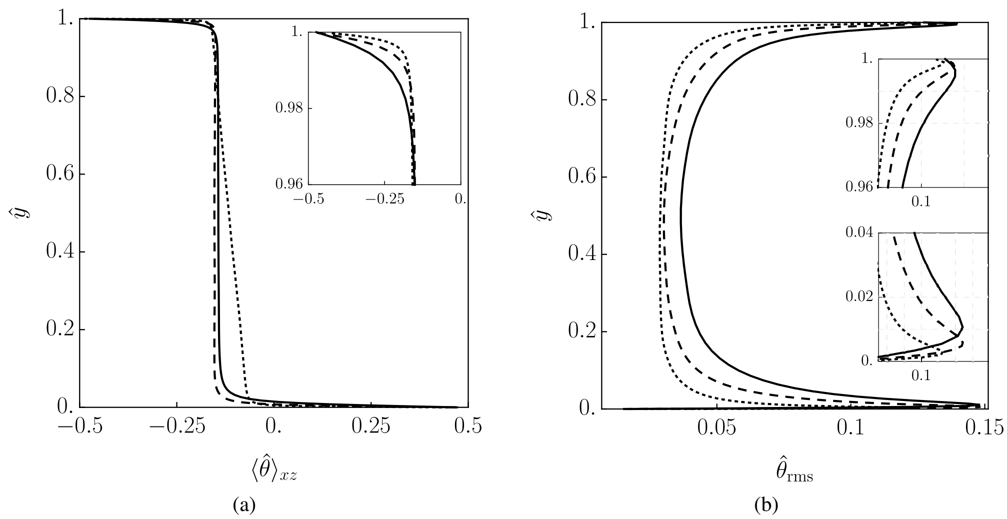

FIG. 16. Temperature plots as Ra is increased (Γ is decreased). (a) Time- and area-averaged temperature , $\langle\hat{\theta}\rangle_{xz}$ and (b) rms of the temperature fluctuations, $\hat{\theta}_{\rm rms}$. The legend is as follows: aspect ratio $\Gamma = 1$ at $Ra = 1.3 \times 10^8$ (——), aspect ratio $\Gamma = 1/2$ at $Ra = 1.1 \times 10^9$ (— —) and aspect ratio $\Gamma = 1/4$ at $Ra = 8.8 \times 10^9$ (⋯⋯).

ACKNOWLEDGMENTS

The first and last authors gratefully acknowledge the financial support of Bel V, a subsidiary of the Belgian Federal Agency of Nuclear Control. The second and third authors performed the experimental work within the framework of the DENOPI research program on spent fuel pool loss-of-cooling and loss-of-coolant accidents. They thank the French Government and the National Research Agency for their financial support (contract reference: ANR11–RSNR006). The present research benefited from computational resources made available on the Tier-1 supercomputer of the Fédération Wallonie-Bruxelles, infrastructure funded by the Walloon Region under the grant agreement n$^{\rm o}$ 1117545.

DATA AVAILABILITY STATEMENT

The data that support the findings of this study are available from the corresponding author upon reasonable request.

Appendix: Flow-chart of evaporation algorithm

In Fig. 17 below, we provide the flowchart for the algorithm calculating the temperature gradient at the upper boundary for the time-step $n+1$, that is $\left.\frac{\partial \widetilde{T}}{\partial y}\right|^{\mathrm{n+1}}$.

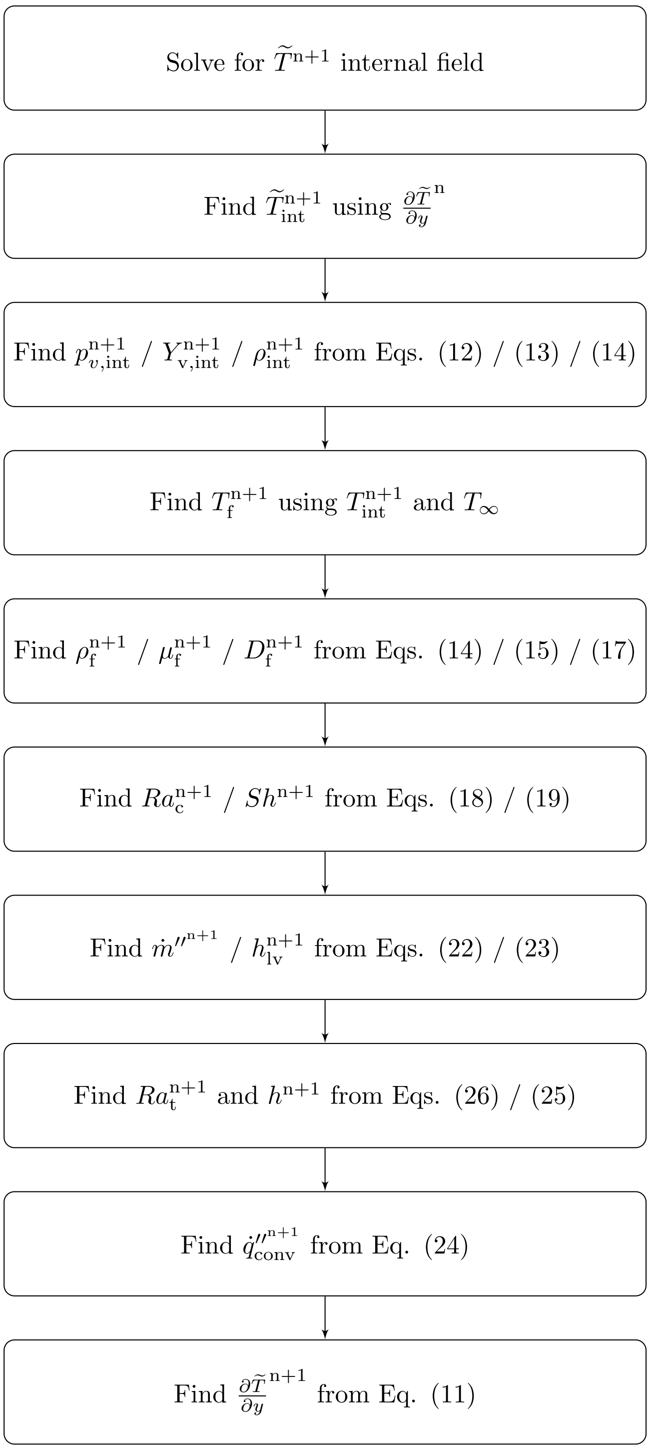

FIG. 17. Flow-chart of evaporation algorithm

[1] W. A. Hay and M. V. Papalexandris, "Numerical simulations of turbulent thermal convection with a free-slip upper boundary," Proc. R. Soc. A **475** (2019).

[2] W. A. Hay and M. V. Papalexandris, "Evaporation-driven turbulent convection in water pools," J. Fluid Mech. (2020), In print.

[3] E. D. Siggia, "High Rayleigh number convection," Annu. Rev. Fluid Mech. **26**, 137–168 (1994).

[4] G. Ahlers, S. Grossmann, and D. Lohse, "Heat transfer and large scale dynamics in turbulent Rayleigh–Bénard convection," Rev. Mod. Phys. **81**, 503–537 (2009).

[5] D. Lohse and K. Xia, "Small-scale properties of turbulent Rayleigh–Bénard convection," Annu. Rev. Fluid Mech. **42**, 335–364 (2010).

[6] W. A. Hay, V. Deledicque, and M. V. Papalexandris, "Numerical simulations of turbulent Rayleigh-Bénard convection with a free surface," in *18th International Topical Meeting on Nuclear Reactor Thermal Hydraulics* (American Nuclear Society, Portland, Oregon, 2019) pp. 14–28.

[7] C. Sun, Y.-H. Cheung, and K. Xia, "Experimental studies of the viscous boundary layer properties in turbulent Rayleigh–Bénard convection," J. Fluid Mech. **605**, 79–113 (2008).

[8] W. G. Spangenberg and W. R. Rowland, "Convective circulation in water induced by evaporative cooling," Phys. Fluids **4**, 743–750 (1961).

[9] K. B. Katsaros, W. T. Liu, J. A. Businger, and J. E. Tillman, "Heat transport and thermal structure in the interfacial boundary layer measured in an open tank of water in turbulent free convection," J. Fluid Mech. **83**, 311–335 (1976).

[10] K. A. Flack, J. R. Saylor, and G. B. Smith, "Near surface turbulence for evaporative convection," Phys. Fluids **13**, 3338–3345 (2001).

[11] S. J. K. Bukhari and M. H. K. Siddiqui, "Turbulent structure beneath air-water interface during natural convection," Phys. Fluids **18**, 035106 (2006).

[12] O. Zikanov, D. N. Slinn, and M. R. Dhanak, "Turbulent convection driven by surface cooling in shallow water," J. Fluid Mech. **464**, 81–111 (2002).

[13] M. Quinn-Brewster, "Evaporation of water at high mass-transfer rates by natural convection air flow with application to spent-fuel pools," Int. J. Heat Mass Transf. **116**, 703–714 (2018).

[14] J. Martin and B. Migot, "Experimental study of the surface evaporation rate of a heated water pool at high temperature using infrared thermography," in *18th International Topical Meeting on Nuclear Reactor Thermal Hydraulics* (American Nuclear Society, Portland, Oregon, 2019) pp. 2302–2313.

[15] A. H. Woodcock, "Surface cooling and streaming in shallow, fresh, and salt water," J. Mar. Res. **4**, 153–161 (1941).

[16] A. H. Woodcock and H. Stommel, "Temperatures observed near the surface of a fresh-water pond at night," J. Met. **4**, 102–103 (1947).

[17] S. M. Bower and J. R. Saylor, "A study of the Sherwood–Rayleigh relation for water undergoing natural convection-driven evaporation," Int. J. Heat Mass Tran. **52**, 3055–3063 (2009).

[18] L. M. K. Boelter, H. S. Gordon, and J. R. Griffin, "Free evaporation into air of water from a free horizontal quiet surface," Ind. Eng. Chem. **38** (1946).

[19] G. Stringano and R. Verzicco, "Mean flow structure in thermal convection in a cylindrical cell of aspect ratio one half," J. Fluid Mech. **548**, 1–16 (2006).

[20] N. Foroozani, J. J. Niemala, V. Armenio, and K. R. Sreenivasan, "Influence of container shape on scaling of turbulent fluctuations in convection," Phys. Rev. E **90**, 063003 (2014).

[21] N. Foroozani, J. J. Niemela, V. Armenio, and K. R. Sreenivasan, "Reorientations of the large-scale flow in turbulent convection in a cube," Phys. Rev. E **95**, 033107 (2017).

[22] H. D. Xi and K. Q. Xia, "Flow mode transitions in turbulent thermal convection," Physics of Fluids **20**, 055104 (2008).

[23] H. D. Xi, Y. B. Zhang, J. T. Hao, and K. Q. Xia, "Higher-order flow modes in turbulent Rayleigh–Bénard convection," J. Fluid Mech. **805**, 31–51 (2016).

[24] S. Weiss and G. Ahlers, "Turbulent Rayleigh–Bénard convection in a cylindrical container with aspect ratio $\Gamma = 0.50$ and Prandtl number Pr = 4.38," J. Fluid Mech. **676**, 5–40 (2011).

[25] P. Koltai and S. Weiss, "Diffusion maps embedding and transition matrix analysis of the large-scale flow structure in turbulent Rayleigh–Bénard convection," Nonlinearity **33**, 1723–1756 (2020).

[26] A. Majda and J. Sethian, "The derivation and numerical solution of the equations for zero-Mach number combustion," Combust. Sci. Technol. **42**,

185–205 (1985).

[27]B. Lessani and M. V. Papalexandris, “Time accurate calculation of variable density flows with strong temperature gradients and combustion,” J. Comput. Phys. **212**, 218–246 (2006).

[28]M. Georgiou and M. V. Papalexandris, “Direct numerical simulation of turbulent heat transfer in a T-junction,” J. Fluid Mech. **845**, 581–614 (2018).

[29]M. V. Papalexandris, “On the applicability of Stokes’ hypothesis to low-Mach-number flows,” Continuum Mech. Therm. (2019), 10.1007/s00161-019-00785-z.

[30]E. W. Lemmon, M. L. Huber, and M. O. McLinden, *NIST Standard Reference Database 23: Reference Fluid Thermodynamic and Transport Properties - REFPROP*, National Institute of Standards and Technology, Standard Reference Data Program, Gaithersburg, 9th ed. (2010).

[31]C. M. Rhie and W. L. Chow, “Numerical study of the turbulent flow past an airfoil with trailing edge separation,” AIAA **21** (1983).

[32]H. G. Weller, G. Tabor, H. Jasak, and C. Fureby, “A tensorial approach to computational continuum mechanics using object-oriented techniques,” Comput. Phys. **12**, 620–631 (1998).

[33]B. Lessani and M. V. Papalexandris, “Numerical study of turbulent channel flow with strong temperature gradients,” Int. J. Numer. Method. H **18**, 545–556 (2008).

[34]R. I. Issa, “Solution of the implicitly discretized fluid flow equations by operator-splitting,” J. Comp. Phys. **62**, 40–65 (1985).

[35]P. J. Oliviera and R. I. Issa, “An improved PISO algorithm for the computation of buoyancy driven flows,” Numer. Heat Tr. B-Fund **40**, 473–493 (2001).

[36]T. M. Eidson, “Numerical simulation of the turbulent Rayleigh–Bénard problem using subgrid modelling,” J. Fluid Mech. **158**, 245–268 (1985).

[37]W. H. Cabot, “Large-Eddy Simulations of time-dependent and buoyancy-driven channel flows,” in *Annual Research Briefs, 1992* (1993) pp. 45–60.

[38]S. Kenjereš and K. Hanjalić, “LES, T-RANS and hybrid simulations of thermal convection at high ra numbers,” International Journal of Heat and Fluid Flow **27**, 800–810 (2006).

[39]J. Smagorinsky, “General circulation experiments with the primative equations: I. The basic experiment,” Mon. Weather Rev. **91**, 99–164 (1963).

[40]D. K. Lilly, “On the numerical simulation of buoyant convection,” Tellus XIV **14**, 148–172 (1962).

[41]P. Orlandi and G. F. Carnevale, “Large Eddy Simulations of stratified flows,” in *Proceedings of the Isaac Newton Institute Symposium / ERCOFTAC workshop held in Cambridge, U.K.*, Vol. 7, edited by P. R. Voke, N. D. Sandham, and L. Kleiser (Springer, Dordrecht, 1999) pp. 25–38.

[42]C. Meneveau, T. S. Lund, and W. H. Cabot, “A Lagrangian dynamic subgrid-scale model of turbulence,” J. Fluid Mech. **319**, 353–385 (1996).

[43]M. Germano, “Turbulence: the filtering approach,” J. Fluid Mech. **238**, 325–336 (1992).

[44]B. E. Poling, J. M. Prausnitz, and J. P. O’Connell, *The properties of gases and liquids* (McGraw Hill, 2001).

[45]W. Wagner, *A New Correlation Method for Thermodynamic Data Applied to the Vapor Pressure Curve of Argon, Nitrogen and Water* (IUPAC Thermodynamic Tables Project Centre, Department of Chemical Engineering and Chemical Technology, Imperial College of Science and Technology, 1977).

[46]C. R. Wilke, “A viscosity equation for gas mixtures,” J. Chem. Phys. **18**, 517–519 (1950).

[47]T. R. Marrero and E. A. Mason, “Gaseous diffusion coefficients,” Journal of Physical and Chemical Reference Data **1**, 3–118 (1972).

[48]J. H. Lienhard, IV and J. H. Lienhard, V, *A Heat Transfer Textbook*, 5th ed. (Dover Publications, Mineola, NY, 2019).

[49]D. S. Viswanath and N. R. Kuloor, “On a generalized Watson’s relation for latent heat of vaporisation,” Can. J. Chem. Eng. **45**, 29–31 (1967).

[50]J. R. Lloyd and W. R. Moran, “Natural convection adjacent to horizontal surface of various planforms,” J. Heat Transfer **96**, 443–447 (1974).

[51]E. A. Mason and S. C. Saxena, “Approximate formula for the thermal conductivity of gas mixtures,” Phys. Fluids **1**, 361–369 (1958).

[52]O. Shishkina, R. Stevens, S. Grossmann, and D. Lohse, “Boundary layer structure in turbulent thermal convection and its consequences for the required numerical resolution,” New J. Phys. **12**, 075022 (2010).

[53]G. Grötzbach, “Spatial resolution requirements for direct numerical simulation of the Rayleigh–Bénard convection,” J. Comput. Phys. **49**, 241–264 (1983).

[54]R. Stevens, R. Verzicco, and D. Lohse, “Radial boundary layer structure and Nusselt number in Rayleigh–Bénard convection,” J. Fluid Mech. **643**, 495–507 (2010).

[55]H. Tennekes and J. Lumley, *A first course in turbulence* (MIT Press, Cambridge, MA, 1972).

[56]S. H. Peng, K. Hanjalic, and L. Davidson, “Large-Eddy Simulation and deduced scaling analysis of Rayleigh–Bénard convection up to $ra = 10^9$,” J. Turbul. **7** (2006).

[57]R. M. Kerr, “Rayleigh number scaling in numerical convection,” J. Fluid Mech. **310**, 139–179 (1996).

[58]Y.-B. Xin and K. Xia, “Boundary layer length scales in convective turbulence,” Phys. Rev. E **56**, 3010–3015 (1997).

[59]J. D. Scheel and J. Schumacher, “Local boundary layer scales in turbulent Rayleigh-Bénard convection,” J. Fluid Mech. **758**, 344–373 (2014).

[60]F. Chillá, M. Rastello, S. Chaumat, and B. Castaing, “Long relaxation times and tilt sensitivity in Rayleigh–Bénard turbulence,” Eur Phys J. B **40** (2004), 10.1140/epjb/e2004-00261-3.

[61]S. Wagner and O. Shishkina, “Aspect-ratio dependency of Rayleigh–Bénard convection in box-shaped containers,” Phys. Fluids **25**, 085110 (2013).

[62]E. P. Van der Poel, R. J. A. M. Stevens, and D. Lohse, “Connecting flow structures and heat flux in turbulent Rayleigh–Bénard convection,” Phys. Rev. E **84**, 045303 (2011).

[63]J. J. Niemala, L. Skrbek, K. R. Sreenivasan, and R. J. Donnelly, “Turbulent convection at very high Rayleigh numbers,” Nature **404**, 837–840 (2000).

[64]R. Verzicco, “Turbulent thermal convection in a closed domain: viscous boundary layer and mean flow effects,” Eur. Phys. J. B **35**, 133–141 (2003).

[65]R. Verzicco and R. Camussi, “Numerical experiments on strongly turbulent thermal convection in a slender cylindrical cell,” J. Fluid Mech. **477**, 19–49 (2003).